Shape optimization of wind turbine blades using panel methods

Master of Science thesis

A.S. Bravo

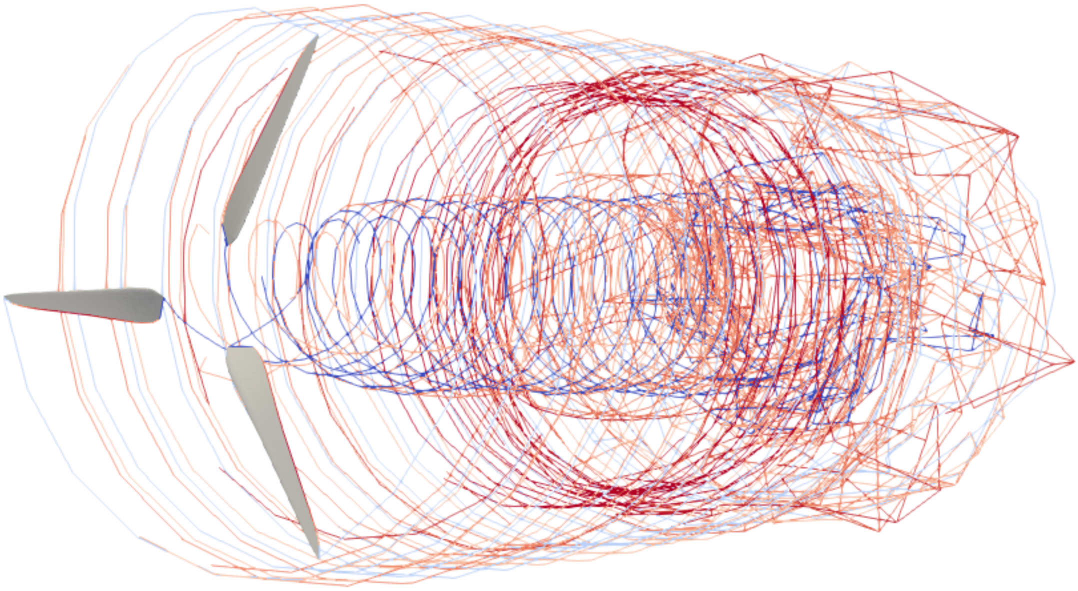

Shape optimization of wind turbine blades using panel methods

Master of Science thesis

by

A.S. Bravo

to obtain the degree of:
Master of Science in Aerospace Engineering at Delft University of Technology
Master of Science in Engineering (Eurpoean Wind Energy) at Technical University of Denmark
to be defended publicly on Monday August 16, 2021 at 9:00h.

Student number TU Delft:	5130581	
Student number DTU:	s193081	
Project duration:	November 1, 2020 – July 31, 2021	
Supervisors:	Professor Ole Sigmund,	DTU
	Associate professor Sergio Turteltaub,	TU Delft
	Postdoctoral researcher Cian Conlan-Smith,	DTU
	Associate professor Casper Schousboe Andreasen,	DTU

Abstract

Wind turbines play an increasingly imporant role in the energy production of our time. In order to optimize the performance of wind turbine blades, this thesis work aims at assessing the possibility of using panel methods for gradient based optimization of the aerodynamics of wind turbine blades. Specifically, the method employed has used Dirichlet boundary condition, a fixed wake for optimization and a free wake model for validation. The panel method developed has been validated against the MIRAS software and CFD results. The results of the optimization are compared against the Glauert optimum blade. The blade is parameterized using NACA profiles and the twist and chord are used as design variables. Two optimizations have been performed: an unconstrained optimization, which has shown to take advantage of limitations of the panel method model; a second optimization is performed applying a thrust constraint and with tighter bounds on the designs variables, which is capable of achieving realistic results. The main conclusion is that realistic blade designs can be achieved using a fixed wake panel method for aerodynamic optimization, although ultimately the performance of these designs should be assessed using higher fidelity models.

Preface

This thesis marks the end of my two year education programme as student of the European Wind Energy Master in the Rotor Design track - Structures. I have learned a lot during this period of time, but above all it has been a period of huge personal development. For this I need to thank all the fellow students of the EWEM programme, who have shared this unique experience with me, and also everyone involved in the organization of the programme; creating a master among four universities is no easy task, but you sure are doing a good job at it.

The Msc thesis itself has been the culmination of this 2 year programme, and as well as the programme itself it has been a joint effort of the universities of DTU and TU Delft. I'd like to thank the thesis supervisors from both universities: Sergio Turteltaub from TU Delft and Ole Sigmund, Casper Schousboe Andreasen and Cian Conlan-Smith from DTU for sharing their time and experience with me. The regular meetings held throughout the past 9 months have been invaluable to keep the thesis going on the right path.

Finally, I would like to thank everyone who has encouraged me in any way in the course of this thesis work. To this regard, I would like to thank my parents for their inconditional support. Also, I appreciate incredibly the daily morning coffees with Thomas, offline and online, which have kept going during the whole duration of the thesis. It was the motor of my days, thank you for that.

A.S. Bravo
Kongens Lyngby, July 2021

List of Figures

List of Tables

Nomenclature

Acronyms

AEP	Annual Energy Production
BEM	Blade Element Momentum
CFD	Computational Fluid Dynamics
COE	Cost of Energy
CoP	Coefficient of Power
DNS	Direct Numerical Simulation
FD	Finite Difference
LES	Large Eddy Simulation
MDO	Multidisciplinary Design Optimization
MMA	Method of Moving Asymptotes
RANS	Reynolds Averaged Navier-Stokes
TP	Trefftz Plane
TSR	Tip Speed Ratio
VLM	Vortex Lattice Method
WT	Wind Turbine

Symbols

Ω	Angular speed of the rotor
$\mathbf{n}$	Vector normal to panel
$\mathbf{q}$	Velocity vector
$\mathbf{r}$	Position in body centered coordinate system
$\mathbf{v}_{\infty}$	Inflow velocity at the rotor
$\mathbf{v_p}$	Perturbed velocity
$\mathbf{v_{ref}}$	reference velocity

μ	Doublet strength
Φ	Potential of the velocity
ρ	Air Density
σ	Dynamic viscosity/Source strength
A_i	Doublet influence coefficient of blade and wake
B_i	Source Influence coefficient
c	Reference length (chord)
C_i	Doublet influence coefficient of blade/wake
C_P	Pressure coefficient
f	Body force
g	acceleration of gravity
Re	Reynolds number
S_B	Body surface
S_rot	Rotor area
S_W	Wake surface
sf	shortening factor; related to wake length
u	speed in the x direction.
v	Speed in the y direction.
w	Speed in the z direction.
a	axial induction factor
a’	Tangential induction factor
B	number of rotor blades
p	Pressure

Contents

1

Introduction

It is undeniable that wind turbines play a major role in the energy production of our time; in 2019 the electricity produced by wind turbines alone represented 15% of the total energy consumed in the European Union [Wind Europe, 2020] and it is foreseen that the share of wind in the energy market will continue to increase [IEA, 2020, GWEC, 2020]. There is much focus in the optimization of wind turbines to make them more efficient and be able to drive the cost of energy down in order to make this form of energy more competitive in the market. Specifically, blades represent a very important share of the cost of manufacturing a wind turbine, and the energy production itself highly depends on them. Multidisciplinary Design Optimization (MDO) is a growing approach because it is necessary to achieve trade-offs between the aerodynamics and structure of the blade to achieve an optimum design. Considering only aerodynamic motivations, the airfoils would be chosen to be thin to be able to maximize power extraction. However, this is not possible because the structure requires thicker airfoils, specially close to the root, to be able to fulfill the requirements of tip displacement and bending moments, among others [Bottasso et al., 2016]. In this sense, it is important to perform mulditidciplinary optimization of wind turbine blades, as opposed to sequential monodisciplinary optimizations, in order to improve the design of wind turbine blades.

The aerodynamic design variables in MDO can range from chord and twist distribution of the profiles [Bottasso et al., 2016] to full shape optimization of a WT blade, including the shape of the airfoils in the design, as in Kenway et al. [2010], Bottasso et al. [2014], Madsen et al. [2019]. For the structural part, one choice is to use the size and position of some pre-assumed elements such as spars, cap spars, trailing edge reinforcement, etc. and optimize those. One example, out of many in the literature, is Sessarego and Shen [2018] which preassumes a box-spar shape of the inner structure. The problem of this approach is that it makes use of the structural elements that are already known and being used at the moment, thus limiting considerably the design space. An attempt for a more general approach in the structural design was made by Wang et al. [2020]: the blade was discretized by a 1D beam in the longitudinal direction while at different spanwise sections of the blade 2D topology optimization was performed. In the aerospace field, James et al. [2014] goes further and performs topology optimization on a full wing using 3D brick elements. However, both approaches face the same obstacle: the meshes employed to discretize the structure of the blade and wing, respectively, do not have enough resolution to see any actual substructures like spars or ribs arise. The 2D topology approach from Wang et al. [2020] has the further drawback that neighbouring sections are connected only through a beam model, thus making the appearance of 3D substructures difficult.

After reviewing the work done by other authors in the past in the literature, to the knowledge of the author, multidisciplinary optimization has not been performed on wind turbine blades using a gradient based approach. The aim of this thesis work is to start to cover this gap. Specifically, this project will build on the previous work carried in DTU by Cian Conlan-Smith as part of his doctoral thesis. In the article Conlan-Smith et al. [2020] the aerodynamic shape of an aircraft wing was optimized using a panel method as aerodynamic model. On later work [Conlan-Smith and Schousboe Andreasen, 2020] MDO optimization of an aircraft wing performing simultaneous aerodynamic and structural optimization adding a Timoshenko beam model to the panel method to calculate the structural displacements and loads.

The objective of this thesis work is to optimize the aerodynamic shape of a wind turbine blade using a panel method and a gradient based search algorithm, and test whether panel methods are an appropriate tool to be used for MDO in wind turbine blade design.

The report is structured as follows: chapter 2 makes a review of the existing literature on multidisciplinary optimization and specifically on aerodynamic modelling of wind turbines; chapter 3 presents the aerodynamic model employed and a validation of it; chapter 4 presents Glauert's optimal rotor, which will be used later on as benchmark of comparison for the optimization results; chapter 5 presents the results of the aerodynamic optimization and compares them against the Glauert rotor presented previously; finally, chapter 6 concludes the thesis project and gives advice on how to proceed with the established work.

2

Literature Study

In the introduction chapter the most relevant work similar to this project was described briefly. An important part of the challenge of WT optimization lays in making an appropriate choice of methods for the optimization. In the following sections the most common choices in the literature are outlined, which will later help motivate the choice of methods for this thesis project. Specifically, the topics touched upon are: the choice of an appropriate objective function for optimization, the search strategy of the design space and the aerodynamic model used to compute aerodynamic loads.

2.1. Choice of objective

When performing simultaneous aerodynamic and structural optimization one has to make a choice of objectives for the optimization. One option is to perform multi-objective optimization, improving at the same time aerodynamic and structural variables. This is the approach chosen in Fischer et al. [2014], where Thrust, Mass and Annual Energy Production (AEP) are optimized simultaneously. A different direction is to try to convert the several competing objectives into a single one, for example using a weighted sum of the objectives as the problem objective. Wang et al. [2020] applies this approach using different weights for the power coefficient C_p and the structural compliance. A popular approach, essentially equivalent to the weighted sum, is to use the Cost of Energy (COE) as figure of merit, employed for example in Bottasso et al. [2016] and Ashuri et al. [2014]. This approach tries to take into account in one single function the combination of the cost of manufacturing, transport, maintenance, etc. of the wind turbine and the expected energy output. The Cost of Energy is the real driving factor in industry when designing a wind turbine. However, determining the cost function of a wind turbine can be tricky when performed in an automatic optimization approach since some of the costs are difficult to obtain [Bottasso et al., 2016].

2.2. Exploration of the design space

There are several strategies in which the design space can be explored. A popular option is to use gradient-free approaches such as Evolutionary Algorithms [Fischer et al., 2014, Vianna Neto et al., 2018]. Evolutionary Algorithms are very good at exploiting non-smooth design spaces, are in general easy to implement and are very well suited for multi-objective optimization. However, they tend to be slow and show poor convergence. Gradient-based approaches [Bottasso et al., 2016, Wang et al., 2020] are comparatively more complex to implement and explore a narrower region of the design space, but are computationally much more efficient and need fewer iterations to converge, which is why they are deemed more appropriate for high-fidelity implementations. On the other side, gradient-based approaches have a tendency to get stuck around local optima and are sensitive to the initial conditions. Still another approach is surrogate modelling, as used by Sessarego and Shen [2018]. By feeding several blade designs to the algorithm, for which each of them the mass is optimized in an inner loop, a simplified explicit function of the Cost of Energy on the design variables is found. In this case the design variables being the chord, twist and relative thickness of the blade. The maximum of the COE simplified function is then found by a grid search approach, which ensures that the global optimum will be found.

2.3. Aerodynamic models

The objective of this subsection is to give an overview of the aerodynamic models that are employed for load calculation on wind turbine blades. In the future this information will help motivate the choice of an aerodynamic method for the aerostructural optimization of a wind turbine blade.

The aerodynamic models that are more used for load calculation on wind turbines are listed below:

- Blade Element Momentum (BEM)
- Vortex Methods
- Euler
- Reynolds Averaged Navier-Stokes (RANS)
- Large Eddy Simulation (LES)
- Direct Numerical Simulation (DNS)

The methods are organized from lower fidelity to higher fidelity, and from low to high computational cost, starting from BEM up until DNS. A brief overview of these methods, including its main strengths and weaknesses, will be presented in the following alineas. The reader is referred to Hansen et al. [2006] for a more thorough overview on the topic.

The momentum theory was first developed by Rankine and Froude, and extended by Glauert to account for 2D effects. The rotor is modelled by an actuator disc, divided into concentric annular streamtubes. The streamtubes are assumed to be independent from each other and the number of blades is assumed to be infinite. The theory makes use of the fundamental principles of mass conservation, axial and angular momentum balances and energy conservation to every control volume (streamtube); added to the blade element theory, the local flow conditions can be calculated assuming that the 2D profiles of the blade act independently of surrounding elements. The combined approach, which we call BEM theory, allows the calculation of the aerodynamic forces and the induced velocities at the rotor. The BEM theory is limited to axial induction factors of 0.5; however, this can be extended for a higher range of induction factors with the introduction of empirical formulas [Wang, 2012]. Similarly, several corrections have been introduced over the years to account for effects of stall delay, dynamic stall, stall misalignment, etc. [Thé and Yu, 2017].

BEM is the most used design tool seen in the literature for optimization purposes [Madsen et al., 2019]. It combines mass and momentum balance equations on the rotor with 2D airfoil data at specific spanwise positions of the blade to obtain loads in every spanwise position. The reason why it is so popular is because of its easy implementation and low computational cost. However, it also has many deficiencies. The flow is assumed to stay within so called stream tubes, so it can't model 3D rotational effects. Other phenomena like yaw misalignment, dynamic stall, etc. are only accounted for using semiempirical corrections. Additionally, it must be noted that due to some of its assumptions the effects of non-planar blade geometries (e.g. blade pre-bend or tip winglets) cannot be accounted for [Lawton and Crawford, 2014]. For more information on the BEM theory the reader can refer to Hansen [2015].

Vortex methods model the aerodynamics of a blade (or wing) based on vortices. The influence of these vortices is calculated using the Biot-savart law. Vortex methods can in general refer to several models: Lifting Line, Vortex Lattice Method (VLM) , and Panel Methods, which can be used to model the lifting surfaces of a blade and the wake, or only the wake. The wake can be modelled in three different ways: Rigid (or fixed) wake, prescribed wake and free wake models. A rigid wake doesn't take into account the expansion of the wake, a prescribed wake makes use of numerical and experimental analysis to decide on a wake position and free wake models locate the wake based on the effects of all aerodynamic components involved in the model, but doing so results in an increased computational cost [Wang, 2012].

Of the vortex methods mentioned, the focus of this thesis will be put on Panel Methods [Hess, 1973] because of its ability to model 3D surfaces accurately, which is an indispensable requisite of the research formulation in order to be able to optimize the external shape of a wind turbine. The other two methods are limited to small angles of attack and thin airfoils [Peerlings, 2018]. The method is simple to implement and doesn't require a mesh. It gives better insight into the dynamics of the flow than the BEM method, since every element of the blade considered affects every other point of the domain. It is for example possible to calculate cases of yaw misalignment and dynamic inflow [Blondel et al., 2016]. Since vortex methods assume inviscid flow, viscosity and stall are not included in the model and the only source of drag is induced drag. For the same reason rotational augmentation cannot be accounted for, as they arise mainly from perturbations on the viscous boundary layer along the spanwise and chordwise direction due to centrifugal and coriolis forces, respectively. Rotational effects increase the lift coefficient at high angles of attack and cause stall delay, so it is beneficial for the perfomance of the blade [Wang, 2012]. Two aerostructural analyses that have made use in the past of panel methods are Conlan-Smith and Schousboe Andreasen [2020] and James et al. [2014] applied to the optimization of aircraft wings, and Sessarego et al. [2016] for the optimization of wind turbine blades.

RANS is the highest fidelity Computational Fluid Dynamics (CFD) method that still can be used with relative frequency in the wind turbine industry for optimization purposes [Madsen et al., 2019]. As RANS works with time-integrated quantities, it cannot cover all time-dependent phenomena, such as unsteady flow separation and vortex shedding [Thé and Yu, 2017]. Still, it is able to account for viscosity, 3D effects, rotational augmentation and turbulence with an appropriate choice of a turbulence model. However, it is computationally more expensive than BEM and vortex methods, and requires meshing of the 3D domain.

Higher fidelity models are LES, which calculates the effect of large eddies and models the sub gridscale eddies, and DNS, which resolves directly all scales of turbulence. However, they are considered computationally too expensive to be applied to a wind turbine flow field [Wang, 2012], hence they won't be considered further in this review.

3

Aerodynamic modelling

This chapter of the thesis describes the aerodynamic model later employed to carry out the blade optimization. The model is based on the previous work by Cian Conlan-Smith; see references Conlan-Smith et al. [2020], and Conlan-Smith and Schousboe Andreasen [2020], in which aerodynamic and aero-structural optimization of wings was carried out using a panel method code. This thesis aims to build on that work to add capabilities for the load calculation and optimization of rotating blades. Appendix C explains specifically the structure of the software and the additions made in this project.

Section 3.1 explains the basics of potential flow theory and the most important derivations regarding panel methods. Section 3.2 explains the wake model that was implemented for the rotating blade, which is the major change made with respect to the static wing case. Lastly, section 3.3 discusses and compares the results against other aerodynamic models to validate the results of the present code.

3.1. Potential flow theory

This section presents the fundamentals of potential flow theory. Only a brief summary of the theoretical derivations is presented here, in order to put the work of this thesis in context. The derivations are based on the book by Katz and Plotkin [2004]; for further details on the topic the reader is referred to this book.

To characterize the velocity field and loads around a body we will require two sets of equations. The first one is the continuity equation for an incompressible fluid:

$$\nabla \cdot \mathbf{q} = \frac{\partial u}{\partial x} + \frac{\partial v}{\partial y} + \frac{\partial w}{\partial z} = 0 \tag{3.1}$$

The second set of equations are the Navier-Stokes equations, which characterize the motion of a newtonian fluid. They represent the momentum balance on the fluid, thus relating the acceleration with the stresses on the fluid; on the most general form they can be written:

$$\rho\left(\frac{\partial q_i}{\partial t} + \mathbf{q}\cdot\nabla q_i\right) = \rho f_i - \frac{\partial}{\partial x_i}\left(p + \frac{2}{3}\mu\nabla\cdot\mathbf{q}\right) + \frac{\partial}{\partial x_j}\mu\left(\frac{\partial q_i}{\partial x_j} + \frac{\partial q_j}{\partial x_i}\right) \quad (i = 1,2,3) \tag{3.2}$$

Where ρ is the fluid density, is the dynamic viscosity coefficient, p is the pressure. $\mathbf{q}$ is the velocity vector, f is a body force.

However, the Navier-Stokes in its general form do not have an explicit solution; an explicit solution can only be found for very few simplified cases. If we assume inviscid flow we obtain the so-called Euler equation:

$$\frac{\partial \mathbf{q}}{\partial t} + \mathbf{q} \cdot \nabla \mathbf{q} = \mathbf{f} - \frac{\nabla p}{\rho} \tag{3.3}$$

It can be demonstrated via dimensional analysis (see Katz and Plotkin [2004]) that the outer flow around a body can be assumed inviscid for high values of the Reynolds number. The Reynolds number is presented in eq. 3.4, where u here is a reference windspeed and c a reference length, which could be the chord of a blade for the case being. In a high Reynolds flow the inertial forces are in magnitude more relevant than the viscous forces, hence the viscosity can be neglected in the outer region of the flow. However, close to the surface of the blade the shear stresses gain importance and the viscosity can no longer be neglected without affecting the accuracy of the solution.

$$Re = \frac{\rho u c}{\mu} \tag{3.4}$$

A further premise that will be necessary in order to obtain the potential flow equation is the assumption that the flow is irrotational. The definition of rotational flow is tied to the concept of vorticity. For a highly viscous flow, the shear forces are relevant and will cause flow particles to rotate; oppositely, if the shear forces are irrelevant the flow particles will not rotate and the flow can be regarded as irrotational. It can be demonstrated, again, that for high reynolds numbers the generation of vorticity outside of the boundary layer can be neglected, thus it is possible to make the assumption of irrotational flow.

With the condition that the flow is irrotational, the velocity can be written as the differential of a scalar function of the position. This function be called the potential Φ of the velocity:

$$\mathbf{q} = \nabla \Phi \tag{3.5}$$

Then, from eq. (3.1) and (3.5), the Laplace equation is obtained:

$$\nabla \cdot \mathbf{q} = \nabla \cdot \nabla \Phi = \nabla^2 \Phi = 0 \tag{3.6}$$

Solving the Laplace equation gives information about the velocity field around a body. However, in order to calculate the aerodynamic forces around an airfoil, it is necessary to connect the velocity field with the pressure field. For this, the Euler equation (3.3) needs to be used. For an irrotational, incompressible flow, taking gravity as the only conservative force acting on the fluid and in static conditions, the Euler equation can be reduced to the Bernoulli equation:

$$gz + \frac{p}{\rho} + \frac{q^2}{2} + \frac{\partial \Phi}{\partial t} = const. \tag{3.7}$$

The equation tells us that at any given point in space, the left hand side is equal to a constant. Therefore, the left hand side will be equal for a pair of points in space at any chosen moment in time. This will allow later to compute the pressure distribution around a body once the flow around it is resolved.

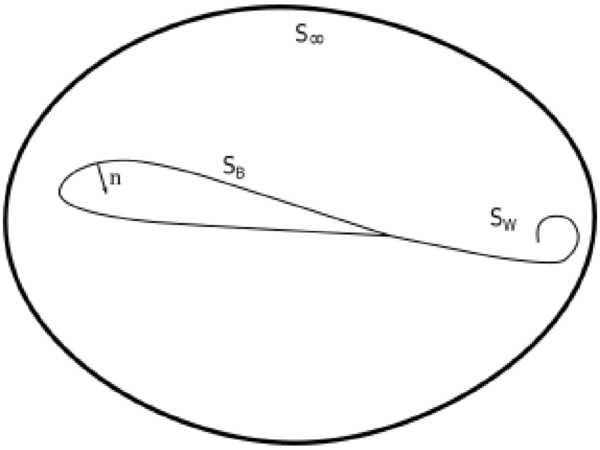

Figure 3.1: Domain and boundaries of interest for the potential flow formulation

Consider the general domain depicted in figure 3.1. Without entering in the theoretical details, the potential at any point of the domain can be written as the integral of the contribution of sources and doublets distributed in the boundaries:

$$\Phi(P) = -\frac{1}{4\pi}\int_{S_B}\left[\sigma\left(\frac{1}{r}\right) - \mu\mathbf{n}\cdot\nabla\left(\frac{1}{r}\right)\right] dS + \frac{1}{4\pi}\int_{S_W}\left[\mu\mathbf{n}\cdot\nabla\left(\frac{1}{r}\right)\right] dS + \Phi_\infty(P) \tag{3.8}$$

In turn, doublets (μ) and sources (σ) are defined as:

$$-\mu = \Phi - \Phi_i \tag{3.9}$$

$$-\sigma = \frac{\partial\Phi}{\partial n} - \frac{\partial\Phi_i}{\partial n} \tag{3.10}$$

Note that the variable μ, which has been used previously in the flow equations, is now used to designate the doublet strength. From now on μ will only be used for this purpose.

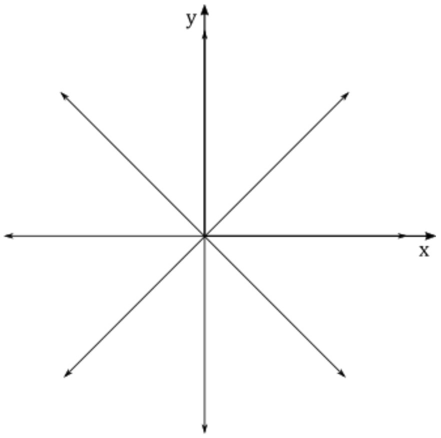

Figure 3.2: Streamlines of a point source.

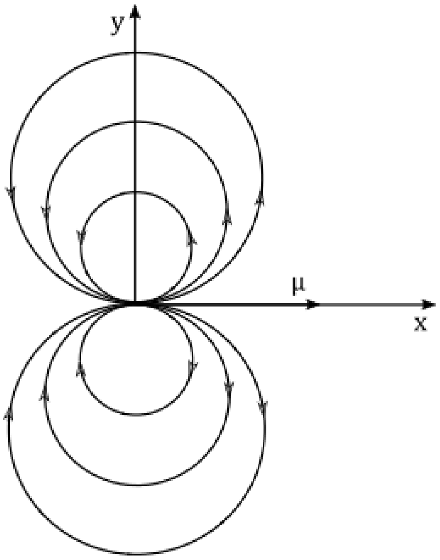

Figure 3.3: Streamlines of a doublet pointing in the x direction.

Doublets and sources are elementary solutions that satisfy the Laplace equation. The velocity field generated by point sources and doublets has been depicted in figures 3.2 and 3.3. It is important to note that the solution to the Laplace equation can be obtained by placing doublets and sources on the boundaries of the problem. In general, though, there is not unique distribution of solutions that will satisfy the Laplace equation, hence a choice based on physical considerations needs to be made.

The problem described above is solved by defining boundary conditions at the surfaces. There are two ways to do this: by enforcing so-called Neumann or Dirichlet boundary conditions. A Neumann boundary condition specifies the value of the derivative of the potential at the surface. This has a directly relatable physical meaning, and it is equivalent to specifying that the velocity normal to the surfaces needs to be zero. Dirichlet boundary conditions, instead, define the value of the potential itself at the boundary. This results in a lower computational cost for the type of problem this thesis works on Conlan-Smith et al. [2020], hence the focus will be put on this second type of boundary conditions.

It can be demonstrated that the inner potential of a closed surface follows the expression:

$$\Phi_i^*(x,y,z) = \frac{1}{4\pi}\int_{S_B+S_W} \mu \frac{\partial}{\partial n}\left(\frac{1}{r}\right) dS - \frac{1}{4\pi}\int_{S_B} \sigma \left(\frac{1}{r}\right) dS + \Phi_\infty = \text{ const.} \tag{3.11}$$

Now, the inner potential can be chosen conveniently ($\Phi_i^* = \Phi_\infty$) so that equation (3.11) reduces to:

$$\frac{1}{4\pi}\int_{S_B+S_W} \mu \frac{\partial}{\partial n}\left(\frac{1}{r}\right) dS - \frac{1}{4\pi}\int_{S_B} \sigma \left(\frac{1}{r}\right) dS = 0 \tag{3.12}$$

Equation (3.12) will be used to reduce the problem to a linear system of equations that can be solved easily by means of well established linear algebra tools, as will be explained next.

3.1.1. Source and doublet strength

Now that the theoretical bases for potential flow have been set, it is necessary to know the numerical procedure to find a solution for a discretized aerodynamic body. For the panel method we are dealing with this means determining the strength of the sources and doublets along the surface.

From the condition that the velocity normal to the surface must be zero (the so-called *Neumann condition*), and the definition of a source (3.10), follows that the strength of a source panel needs to be:

$$\sigma = \mathbf{n} \cdot \mathbf{v_{ref}} \tag{3.13}$$

$$\mathbf{v_{ref}} = [\mathbf{v}_\infty - \Omega \times \mathbf{r}] \tag{3.14}$$

Where $\mathbf{n}$ is normal to the body surface, pointing inside, $\mathbf{v}_\infty$ is the inflow velocity at the rotor, Ω is the angular speed of the wind turbine rotor and $\mathbf{r}$ is the position of a point in body coordinates. $\mathbf{v_{ref}}$ is the flow velocity seen by the body, which is different for every section of the blade.

At this point the strength of the doublets is not uniquely defined. This arises from the fact that infinite values of *circulation*, or equivalently lift, are possible for a given source distribution. To determine the strength of the doublets at each panel, it is necessary to enforce some physical consideration so that the amount of *circulation*, and hence the lift, is the correct one.

The condition that we are going to use is called the *Kutta condition*; it is based on empirical observation, and it essentially states that the flow on an airfoil will leave the trailing edge smoothly. Therefore, as the flow approaches the trailing edge, the velocity at the upper and lower surfaces will need to be equal. Specifically, it is required that the trailing edge is a stagnation point (of zero velocity) when the trailing edge has a finite angle, but a finite velocity can exist for cusped trailing edges. Mathematically, for the case of a panel method using a doublet distribution to generate lift, the Kutta condition can be written as:

$$\mu_U - \mu_L - \mu_W = 0 \tag{3.15}$$

Where the subindices refer to the upper and lower surface of the airfoil and the wake, respectively. Expression 3.15 tells us that there is a jump in circulation at the trailing edge of the airfoil, which is equal to the wake circulation. For further insight on the mathematical development of this expression, the reader is referred to Katz and Plotkin [2004]. Anderson [2017] also covers comprehensively the Kutta condition and its physical explanation. The concept of *circulation*, which has been mentioned here, can also be consulted in these sources.

Additionally to eq. 3.15, the doublets are required to have constant strength along the wake, and the wake shape should be parallel to local streamlines. As will be explained later, when talking about the wake model in section 3.2, it is not immediate how to satisfy this second condition. If the geometry of the wake is prescribed in advance, this condition will be, at best, an approximation. Other methods, which don't require a predetermined wake shape, involve solving the geometry of the wake iteratively until a converged shape that fulfills the physical requirements is achieved.

3.1.2. System of linear equations

Now assume that the body is discretized into N panels, and the wake is discretized into N_W panels. It will also be assumed from now on that the strength of the doublet and the sources in the panels are constant. We can now rewrite equation 3.12 for a discrete body as:

$$\sum_{k=1}^{N} C_k \mu_k + \sum_{\ell=1}^{N_W} C_\ell \mu_\ell + \sum_{k=1}^{N} B_k \sigma_k = 0 \tag{3.16}$$

Equation 3.16 must be true for every panel's *collocation point*. The collocation point is where the boundary condition is enforced; it is located at the center of the panel and slightly inside the body, since the Dirichlet boundary condition (eq. 3.12) needs to be enforced at an inner point of the body. Equation 3.16 expresses that for every collocation point, the sum of the contributions of potential of all the other panels needs to be zero. The contribution of every influencing panel is its *Influence Coefficient* (C_k,C_l,B_k), which depends on its relative position to the collocation point, times the strength of the influencing panel. The influence coefficients are calculated as:

$$C_k = \frac{1}{4\pi} \int_S \frac{\partial}{\partial n} \left(\frac{1}{r} \right) dS \bigg|_k \tag{3.17}$$

$$B_k = \frac{-1}{4\pi} \int_S \left(\frac{1}{r} \right) dS \bigg|_k \tag{3.18}$$

The exact evaluation of these integrals depends on the choice of panel of the model. For constant strength quadrilateral panels, as used in this work, the expressions are derived in Katz and Plotkin [2004], section 10.4.

As seen previously in equation 3.13, the source strengths (σ) can be determined beforehand. The wake doublet strengths can be put as a function of the surface strengths (eq. 3.15). Therefore, the problem of solving eq. 3.12 ultimately corresponds to solving the following system of linear equations:

$$\sum_{k=1}^{N} A_k \mu_k = -\sum_{k=1}^{N} B_k \sigma_k \tag{3.19}$$

Where the matrix A is the matrix C with the contributions from the wake panels.

3.1.3. Load calculation

The total velocity $\mathbf{v_{tot}}$ at a certain point of the body will be the inflow (or reference) velocity (eq. 3.14) plus the perturbation caused by the panels of the body and the wake ($\mathbf{v_p}$):

$$\mathbf{v_{tot}} = \mathbf{v_{ref}} + \mathbf{v_p} \tag{3.20}$$

Now, neglecting the height term and considering that the problem at hand is steady-state (hence $\frac{\partial \Phi}{\partial t} = 0$) eq. 3.7 can be used to compute the coefficient of pressure at every panel of the body:

$$C_P = \frac{p - p_{ref}}{1/2 \rho v_{ref}^2} = 1 - \frac{v_{tot}^2}{v_{ref}^2} \tag{3.21}$$

Note that the reference velocity here used accounts for the rotational speed of the blade and therefore will have a different value for every spanwise location, each section seeing an increasingly high velocity moving towards the tip. Finally, the contribution of a panel to the aerodynamic forces on the body will be:

$$\Delta \mathbf{F} = -C_P \left(\frac{1}{2} \rho v_{\mathrm{ref}}^2 \right) \Delta S \mathbf{n} \tag{3.22}$$

Which if integrated over specific spanwise position will give the normal and tangential forces in that section.

3.1.4. 2D example

Now let's look at the results from a 2D panel method code to better understand what these kinds of methods are capable of and also their limitations. Figure 3.4 shows the C_P distribution over the chord of a NACA 4412 profile for a Reynolds number of $3 \cdot 10^6$. The panel method shows that the C_P distribution follows a similar shape than the experimental data, but it clearly overestimates the suction at the upper side of the airfoil. The main reason behind these differences is the inviscid assumption of the panel method. Since viscosity has been neglected for the theoretical model, the figure shows (as expected) that the lift loads will be overestimated. For higher accuracy, the panels have been placed in a cosine distribution along the chord, so that the mesh is more dense towards the leading edge and the trailing edge. This increases the acccuracy of the solution for a given number of panels, since these are the regions where the C_P suffers more drastic changes.

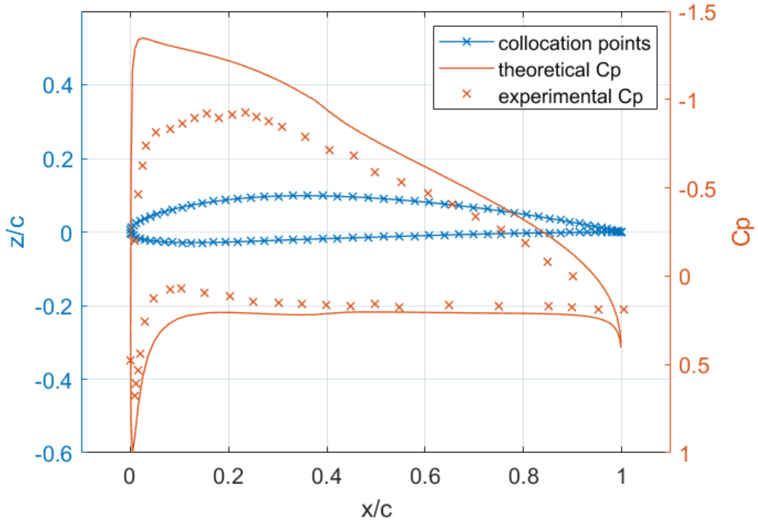

Figure 3.4: Pressure coefficient of a NACA 4412 at an angle of 4 degrees. Results of the 2D implementation of a panel method compared against experimental data. Experimental data extracted from M. Pinkerton [1937]

3.1.5. Modelling of symmetry

The blades of a wind turbine are identical and equally spaced at regular angles. Assuming that the pitch of the blades is also the same, the rotor has rotational symmetry, which can be used to reduce the model that will be employed for the analysis. Only one blade needs to be meshed instead of discretizing the whole rotor. Since the strengths of the singularities will be the same for every blade, the system of equations can also be reduced and has the size of one blade mesh.

The way symmetry is exploited is during the calculation of the influence coefficients. Specifically, blade 1 (schematically represented in figure 3.5) is modelled and solved. For every collocation point of the blade, the influence of the other panels of blade 1 are computed. Then a simple transformation is applied to that panel (eq. 3.23) to find the coordinates of the corresponding panels of blades 2 and 3. While the influence coefficients are still computed for all the panels in the three blades (or any corresponding number of blades), this procedure allows to solve a system of equations of size equal to the panels in one blade. Since solving the system of equations is a very costly part of the program, this allows for a huge decrease in computational cost.

$$\begin{pmatrix} x \\ y \\ z \end{pmatrix}_{k=2,3} = \begin{bmatrix} 1 & 0 & 0 \\ 0 & \cos\Psi_k & -\sin\Psi_k \\ 0 & \sin\Psi_k & \cos\Psi_k \end{bmatrix} \begin{pmatrix} x \\ y \\ z \end{pmatrix}_1 \tag{3.23}$$

3.2. Wake modelling

Three different ways to model the wake of a wind turbine will be distinguished, from lower to higher complexity: *fixed wake*, *prescribed wake* and *free-wake* models. The geometry of a fixed (or rigid) wake is determined as an input and doesn't change during the analysis. It is the simpler model still able to capture the physics of a wind turbine, even though it needs appropriate user input to provide reliable results. A prescribed wake is a simplified model

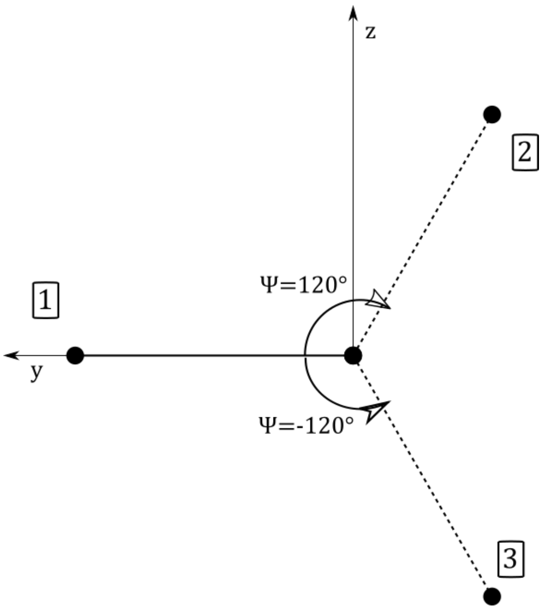

Figure 3.5: Representation of a the wind turbine blade model. Blade number 1 is meshed, while blades 2 and 3 are accounted for via symmetry. The x axis points towards the document, following the right hand rule.

that gives a wake geometry as a function of some simplified parameters. For example, Robison et al. [1995] proposes a model to calculate the wake geometry as a function of the induction at the blades. This allows the implementation of an iterative scheme where the blade induction is updated until convergence. This type of methods are tested and tuned for existing wind turbine data, but it might not be the best approach to testing novel WT geometries [Vermeer et al., 2003]. The third method is the free-wake approach. In this model the interaction between wake filaments/panels is accounted for. The wake shape is computed iteratively until the conditions of equation 3.24 are met. Here below the fixed and free wake methods that have been implemented will be commented on; however, there are several other free wake methods that can be consulted for example in Leishman [2006] and Katz and Plotkin [2004].

3.2.1. General considerations

he governing equations and the resulting system of linear equations used to solve the doublet strength for each panel have been discussed previously in section 3.1. It has also been shown how to compute the wake strength as a function of the trailing edge doublets using the Kutta condition. The effect of the wake has been mentioned there. However, until now the computation of the wake geometry is a topic that has not been touched upon. This subsection will briefly discuss general principles that determine the wake shape.

A doublet panel of the wake should respect the condition that it should not generate lift, because it is not a solid surface (see Katz and Plotkin [2004]), this can be expressed as:

$$\mathbf{q} \times \nabla \mu_W = 0 \tag{3.24}$$

Hence, the boundaries of the wake panels should be parallel to the local velocity. Since the wake geometry is obviously not known beforehand, this will require iterative methods to find a converged solution. The family of methods that attempts to find a wake that follows equation 3.24 are called free wake methods.

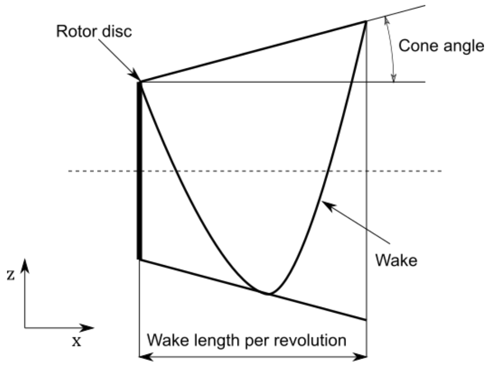

Figure 3.6: Representation of a conical fixed wake model.

3.2.2. Fixed wake

A fixed wake is a model that represents the vorticity shed by the blades independently from the parameters of the model. The geometry is chosen beforehand and is not updated during the design. Therefore, a degree of experience and previous knowledge on wake geometries is required to achieve acceptable results using a fixed wake model.

The implementation of the fixed wake model allows for an improvement of the comprehension on how the wake geometry will affect the loads on the wind turbine. Figure 3.6 shows a representation of the fixed wake employed in the model. The two parameters that can be changed are a cone angle and a length factor, which determines the velocity at which the wake is propagating. Note that it is assumed that the wake panels shed at the same instant will remain in-line —there is no shear parallel to the x direction—.

The parameter sf, which stands for *shortening factor*, is defined below with regards to the fixed wake model, as it will be useful later on.

$$sf = \frac{\bar{u}_{wake}}{u_\infty} \tag{3.25}$$

sf measures the ratio of the speed of the wake and the undisturbed speed. To exemplify this, for $sf = 1$ the wind turbine would not be slowing the wind down at all, while for $sf = 0.5$ the wind turbine is slowing the wind to half the inflow speed.

3.2.3. Free wake

The free-wake model implemented is similar to the method proposed in Katz and Plotkin [2004], referred to as *time-stepping* model for a steady state case. The equation that rules the motion of the panels of the wake is the following one:

$$\frac{\mathrm{d}\mathbf{r}}{\mathrm{d}t} = \mathbf{v_{ref}}(\mathbf{r}) + \mathbf{v_p}(\mathbf{r}) \tag{3.26}$$

where the term $\mathbf{v_{ref}}$ refers to the velocity due to the change in the reference system, and $\mathbf{v_p}(\mathbf{r})$ is the induced (or perturbed) velocity.

Different numerical schemes are possible to solve equation 3.26, namely explicit, hybrid and implicit. Explicit methods are simple conceptually; however, they are prone to numerical issues related with round-off errors (see Leishman [2006], p.618).

Two different methods have been implemented in the present code, both described in Leishman [2006]. The first one is an time-stepping Euler explicit approach. The second one is an approach close to the predictor-corrector scheme described in the former reference, which is a two-step explicit approach.

Let's start by describing the Euler explicit approach. The first iteration is conducted using the fixed wake geometry described in sec. 3.2.2. The velocities are calculated at every point and then every point is propagated using the velocity information:

$$\mathbf{r}^{n+1} = \mathbf{r}^n + \Delta t \cdot \mathbf{v_p}(\mathbf{r}^n) + \Delta \mathbf{r}_{ref} \tag{3.27}$$

Where the term $\Delta\mathbf{r_{ref}}(\mathbf{r}^n)$ accounts for the fact that the body frame of reference is rotating. The superindices n and n+1, respectively, refer to the current and future time steps. In this method the points are trailed based on the velocity calculated at the current position, hence no information of the future step is required and there is no need to solve a system of equations.

Leishman [2006], p.618 suggests that Euler explicit methods do not present consistent convergence, but rather can start oscillating after some iterations. This will be discussed for the present case further down this section. For this reason, a predictor-corrector scheme was implemented for the wake.

The predictor-corrector scheme consists of two explicit stages. In the first stage an approximation of the wake geometry $\tilde{\mathbf{r}}^{n+1}$ is made using eq. 3.28. The geometry at time-step n+1 is then used to approximate the perturbation velocity ($\mathbf{v_p}(\tilde{\mathbf{r}}^{n+1})$). This first stage allows to know the velocity at the future time-step without actually solving a system of equations, as would be the case for an implicit method. The second stage of the predictor-corrector scheme follows eq. 3.29:

$$\tilde{\mathbf{r}}^{n+1} = \mathbf{r}^n + \Delta t \cdot \mathbf{v_p}(\mathbf{r}^n) + \Delta \mathbf{r}_{ref} \tag{3.28}$$

$$\mathbf{r}^{n+1} = \mathbf{r}^n + \Delta t \cdot \big((1-f)\cdot \mathbf{v_p}(\mathbf{r}^n) + f \cdot \mathbf{v_p}(\tilde{\mathbf{r}}^{n+1})\big) + \Delta \mathbf{r}_{ref}(\mathbf{r^n}) \tag{3.29}$$

The parameter f is used to control how much information is used from this time-step and from the estimate of the next time-step. Notice that for $f = 0$ this method would be identical to the forward Euler approach, as described by eq. 3.27; $f = 1$ would correspond to an Euler backwards approach, while $f = 0.5$ is the closest to what is described in Leishman [2006] as the *predictor-corrector approach.* From now on, when mentioning the predictor-corrector approach it will refer to eq. 3.29 with $f = 0.5$ specifically.

A convergence study has been conducted on the wake method developed here, which can be seen in figure 3.7. The residual has been chosen to be:

$$R = \frac{||\mu_{\mathbf{new}} - \mu_{\mathbf{old}}||}{||\mu_{\mathbf{old}}||} \tag{3.30}$$

The convergence criteria has been selected as the doublet strength since this is what is ultimately relevant for the resulting loads. In this run the convergence criteria was set to the residual being below 10^{-4}. Figure 3.7 effectively shows that the forward Euler method presents some oscillating behaviour near the end. The backward Euler doesn't converge at all for the 100 iterations allowed. The predictor-corrector scheme is the one that presents a more consistent convergence. However, note that the predictor-corrector scheme and the backward Euler require to calculate the nodal velocities twice, for $\mathbf{r}^n$ and for $\mathbf{r}^{n+1}$, while the forward Euler only requires the velocities at r^n. The computation of the induced velocities

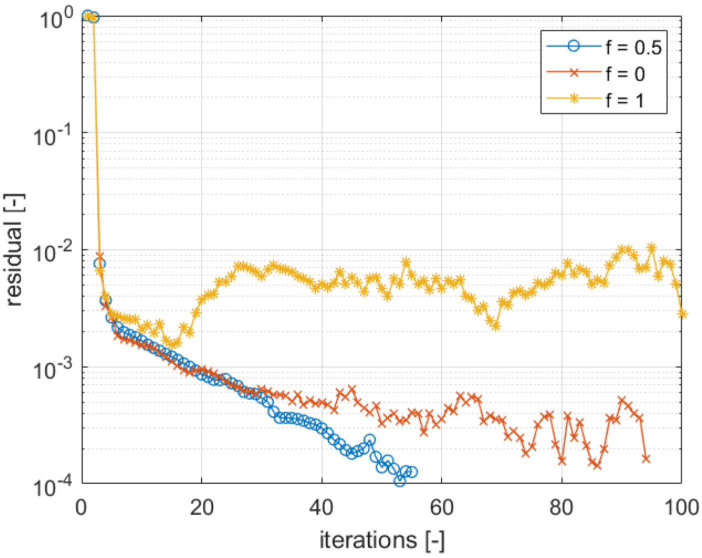

Figure 3.7: Convergence study on the wake model using an Euler forward model $f = 0$, an Euler backward ($f = 1$) and a predictor-corrector scheme ($f = 0.5$).

is a costly computation, which means that doubling this computation represents a considerable increase in the overall running wall-clock time. The Predictor-corrector scheme takes on average ≈ 65% more time per iteration of the wake than the explicit Euler. For most runs, it is considered that a residual of 10^{-3} is enough to consider the code converged. In that range of accuracy, the Euler forward method seems to be the best trade-off between accuracy and computational cost and as such will be the primary choice for the optimization runs.

3.3. Validation of the aerodynamic model

In this section the developed panel code will be compared against the results from the MIRAS software. MIRAS is also a panel method code and has been validated extensively before, which makes it convenient to compare the results of this thesis work against it.

This section will first explain the case that is being used to validate the code, that is the NREL 5MW geometry (see NREL 5MW report by Jonkman et al. [2009]). The next subsection is a comparison of the normal and tangential forces along the blade span, followed by a study on the pressure distribution on some sample sections along the blade. The last subsection is a discussion of the results obtained, which includes a discussion on them with an expert on panel methods, the researcher Néstor Ramos-García, who is the main developer of the MIRAS code.

3.3.1. Validation case study

The results of the simulations of this thesis are compared, specifically, against the article by Ramos-García et al. [2014].

While essentially the presently developed panel code and the MIRAS model are both panel codes, there are some differences in the implementation that must be noted to the reader, which are mentioned hereunder. MIRAS is a computational panel code that uses the Neumann no-penetration condition to enforce the boundary conditions. The present code, on the contrary, uses a Dirichlet BC. The code can be run with and without accounting for viscosity, which is taken into account by coupling the panel code to a viscous boundary layer solver, Q^{3}UIC. The wake is modelled using a free-wake model that employs trailing filaments to account for the influence of the wake on the flow field. Oppositely, the present code uses quadrilateral panels to model the wake.

In the mentioned article, MIRAS is run on several wind turbine rotors. For the present comparison, we will take the results from the analyses on the NREL 5MW rotor. The NREL-5MW is a fictitious wind turbine to be used by researchers, aimed at testing new models and methods of analysis, as well as new technologies, to be able to compare easily the results of those studies on a common-ground wind turbine. The reference turbine is an upwind, variable-speed, pitch controlled machine. The aerodynamic, structural and control parameters necessary for an analysis are provided in the NREL report. The aerodynamic sections are provided at different stages of the blade, along with their corresponding polars ($C_l - \alpha$ and $C_d - \alpha$ plots). Together with the chord and twist values at each section, this is enough to conduct an analysis with a BEM code. However, for CFD or a panel code the exact geometry is needed, which is not provided in the original NREL 5MW report. This is why several researchers who have used this baseline turbine need to take some freedom into deciding how to model the geometry.

For several sections along the blade, the parameters given in the NREL report are *radius*, *chord*, *twist* and the specific *airfoil* used in the section. A further assumption needed is regarding the center of the *blade axis*. It is assumed that the blade axis is straight and that it is located at 25% of the chord for every airfoil section. The twist is therefore applied at each blade center.

The second additional modification has to do with the airfoil shape. The original airfoils (see figure 3.8) which can be found in the original NREL report have blunt trailing edges, which is a problem when running panel method simulations. In these cases, enforcing the Kutta condition is problematic. The kutta condition helps determine the amount of circulation around an airfoil, given that the flow leaves the trailing edge smoothly. This requires the trailing edge to be sharp and no separation to occur. For the case of a blunt trailing edge, it is not obvious where to place the Kutta condition, or if it can be used at all for the aforementioned reasons. Secondly, these flatback profiles have an abrupt change in the geometry near the trailing edge, which can cause numerical issues when computing the C_P of the sections. For these reasons it becomes necessary to modify the aifoils to sharpen the trailing edges. The geometries used for the analysis are shown in figure 3.9, which are the same ones as used for input for the MIRAS runs.

3.3.2. Spanwise loads on the rotor

Now a comparison of the spanwise loads will be presented for three different models: the MIRAS inviscid, the currently developed panel code, and a CFD simulation. The CFD simulation, unlike the panel codes, takes into account viscosity and flow separation. Figure 3.10 shows the load distribution on the NREL 5MW rotor. The normal force, perpendicular to the rotor disc, is related to the total thrust on the wind turbine. The tangential force is perpendicular to the blade axis and in-plane with the rotor disc, hence it is related with the torque and the power produced by the blades.

The results for the normal force are very close for the three models, this is because the normal contribution is mostly dependent on the lift generated by each section, which is

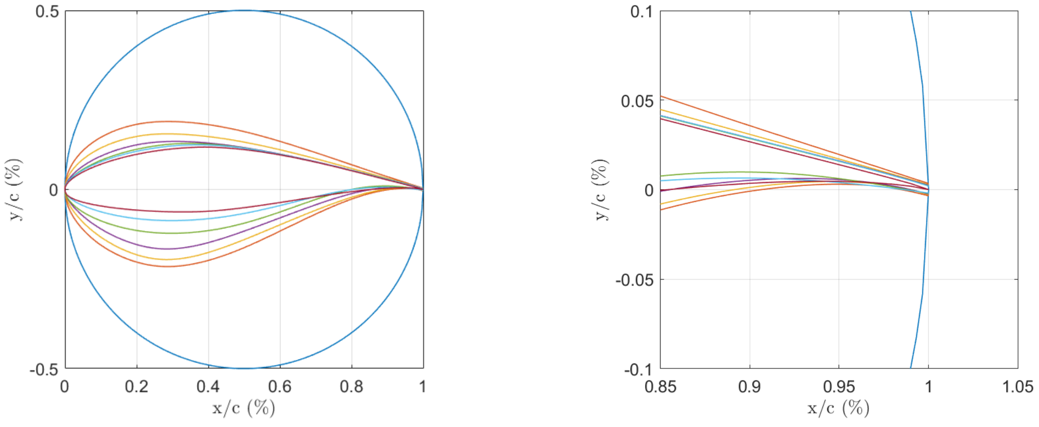

(a) (b)

Figure 3.8: a) NREL 5MW airfoils and b) Zoom on the TE

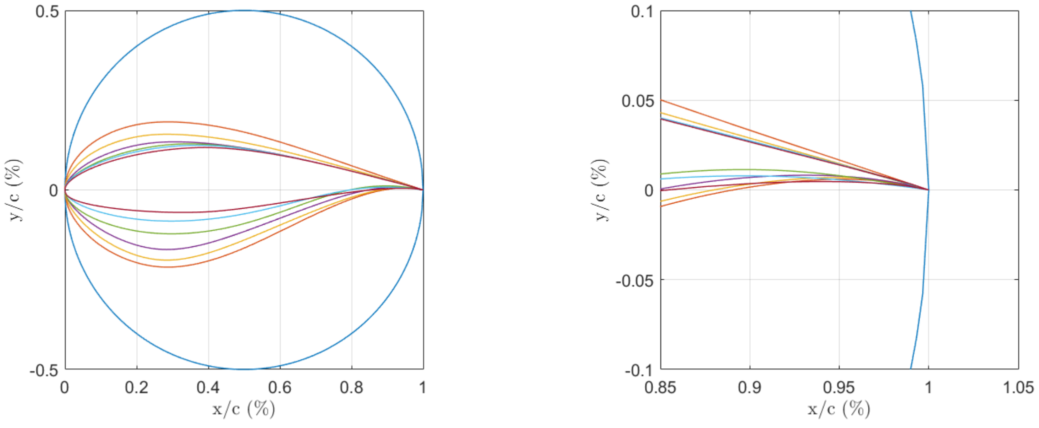

(a) (b)

Figure 3.9: a) Modified NREL 5MW airfoils and b) Zoom on the TE

accurately represented in a panel code.

The results for the tangential force are, however, rather different for the CFD and the two panel codes. Only near the tip, where the tip effects play a major role, do the codes start to have a similar behaviour. The tangential component of the force is more affected by the drag of each section. Since the panel code developed is inviscid, the viscous drag is not accounted for and the tangential force is overpredicted in most of the span. Close to the root an additional effect adds up to the difference between CFD and the panel codes. For similar reasons as mentioned previously for the blunt trailing edge profiles, the Kutta condition is not applicable to cylindrical sections. This causes the cylindrical sections to effectively generate lift, which is nothing but a discretization-driven phenomennon, with no physics behind. This will be commented on further in the next subsection.

Regarding the behaviour of the two panel codes, they are both similar, which gives confidence that there are no major issues in the currently developed code. The only appreciable differences are in the middle sections, where the current code predicts loads slightly under MIRAS, and near the root where it seems to behave a bit more abruptly than the MIRAS code.

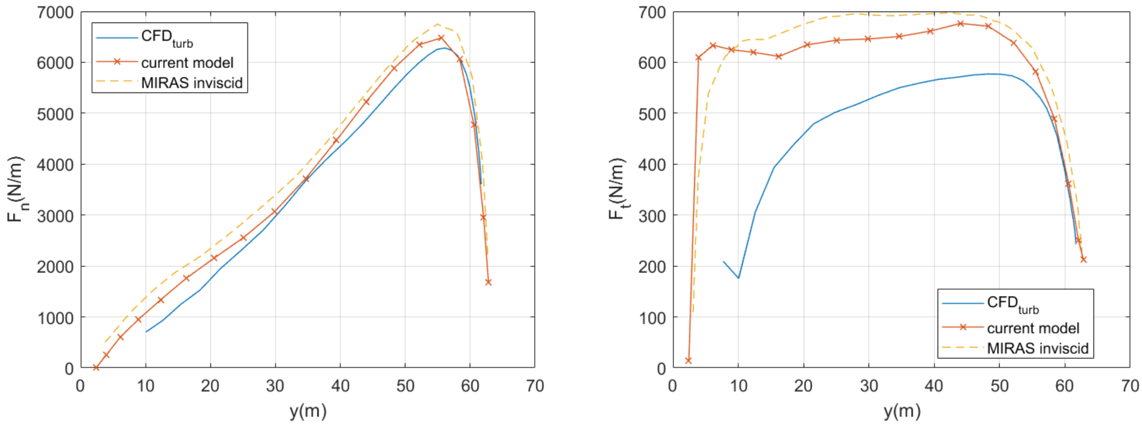

(a) (b)

Figure 3.10: Comparison of normal a) and tangential b) forces on the NREL 5MW rotor blades using CFD , MIRAS and the currently developed code. Extracted from Ramos-García et al. [2014]. The first point from assto has been excluded for visualization purposes.

All in all, what is important to discuss here is whether the panel code will be useful for design purposes. While the power production will be definitely overestimated for the above-mentioned reasons, there is basis to think that it will allow for a sensible design of a wind turbine. For most of the span, the tangential loads are overpredicted but follow a similar trend than that of the CFD results. The exception is close to the root, where the panel code is not able to capture the flow separation that occurs there. The present results point in the direction that this panel code will be able to provide reasonable designs in the middle and tip regions of the blade, which are the most important parts with regards to power production.

3.3.3. Pressure distribution along the span

Figures 3.11-3.16 show the pressure distribution along representative sections of the wind turbine. This allows for further insights into the load distribution that has been commented upon previously. The first thing to notice is that the sections immediately at the root and at the tip present some numerical issues. While this does not cause a big overall change in the WT performance, it is something to be aware of for the further stages of the design. The middle sections of the blade, as well as all other sections not immediately close to the tip or root, on the other hand, present the expected behaviour and show no problems apart from small issues close to the trailing edge.

3.3.4. Discussion on the validation

Additional to the previously made comments, the results of the currently developed code have been discussed with an expert on the field of panel code modelling [Néstor Ramos-García, personal communication, 7th April, 2021]. The following points are a reproduction of what was talked upon in the meeting. Néstor is also the main developer of the MIRAS code, hence some further insights are provided on the differences between the two panel codes.

MIRAS uses a similar method to compute forces, namely C_P integration, and the free wake models employed are not identical but follow very similar principles.

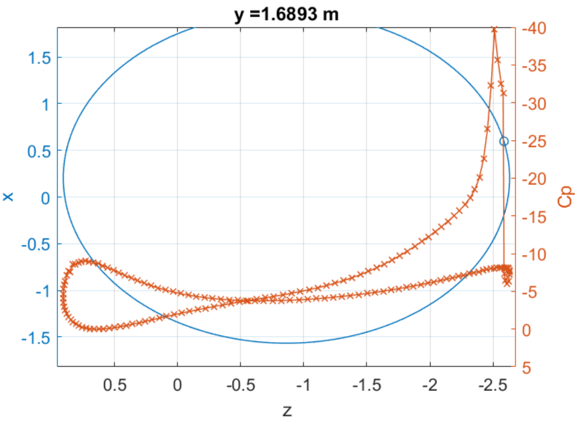

Figure 3.11: Normal force to the rotor along the span

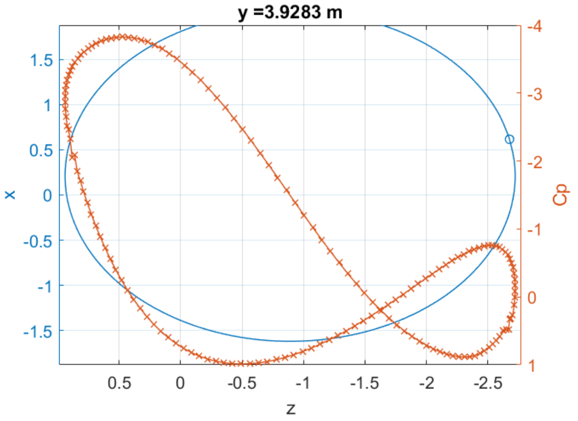

Figure 3.12: Tangential force to the rotor along the span

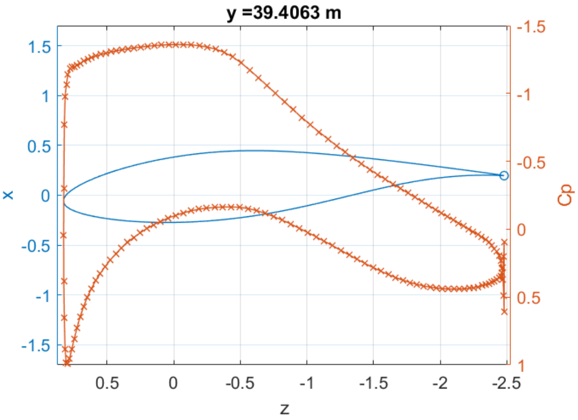

Figure 3.13: Normal force to the rotor along the span

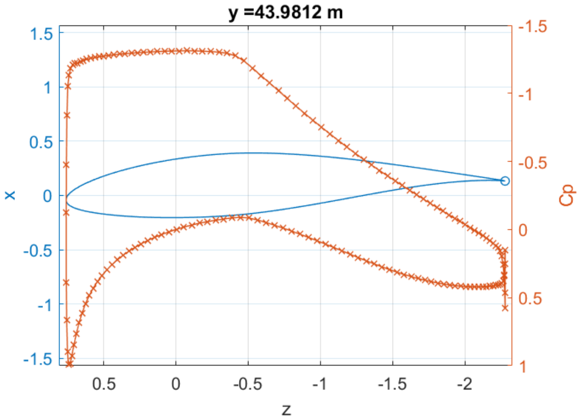

Figure 3.14: Tangential force to the rotor along the span

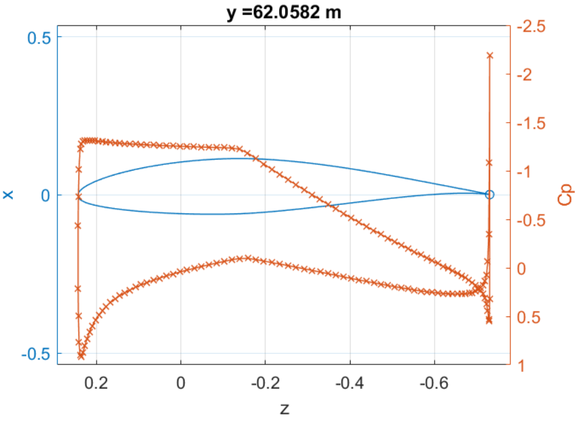

Figure 3.15: Normal force to the rotor along the span

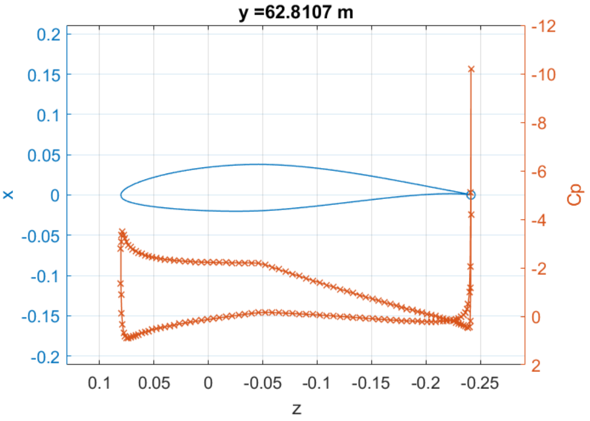

Figure 3.16: Pressure distribution at the tip

The topic on the differences between codes was addressed, namely where do the differences come from for two codes that have very similar implementation. The three major possibilities are small changes of the geometry, changes in the free wake model or changes in the boundary conditions. The wake model differs in how the first row of panels is defined. Furthermore, the wake consists of quadrilateral panels for the current code, while it is modelled by vortex filaments in MIRAS. The boundary condition employed is Dirichlet for the current code, but Neumann for MIRAS. It is also acknowledged that changes in the discretization of the geometry can have significant effect on the results.

The previously mentioned differences in loads at the root (circular and close to circular sections) and in the middle sections can be likely attributed to the mentioned differences.

It remains to be determined the cause of the numerical issues near the root and the tip. Néstor made a suggestion with regards to the topics that have been mentioned so far: Regarding the issues at the cylindrical sections, panel codes seem not to be ready to deal with this issue for the moment. A model that accurately represents the detaching flow for panel methods is yet to be developed. Hence, it is considered normal that the issues are experienced close to the root section. For the purpose of this work, these root sections should better be excluded from the design optimization to avoid undesired numerical issues to appear. A second suggestion from Néstor pointed in the direction of implementing the Neumann boundary condition to the code. This would help rule out the possibility that there are errors in the code, since the choice of boundary conditions is one of the major implementation differences.

4

Glauert’s optimum rotor

In this section a well known optimal rotor design is presented making use of Glauert’s momentum theory. The resulting design will be used as a baseline for future chapters and to increase the understanding of the optimization using panel methods. Additionally, the assumptions of such theory are highlighted to understand which differences might be encountered between the two models.

4.1. Glauert’s Optimal rotor

In the following section the theory behind the optimum rotor, as defined by Glauert [1935], will be described with the purpose to compare the results of the optimization against it. Let’s start by introducing some basic concepts. At every spanwise station of the blade, the contributions of all incoming speeds can be represented as in figure 4.1, where a and a’ represent the induction factors in the axial and the tangential directions, respectively. The induction factors are the non-dimensional axial and tangential velocities induced at the rotor mainly by the lift force, and defined as:

$$a = 1 - \frac{v_a}{v_\infty} \tag{4.1}$$

$$a' = \frac{v_t}{\omega r} - 1 \tag{4.2}$$

The power at a given spanwise location, for a stream tube of width $\mathrm{d}r$, is given by the following expression:

$$\mathrm{d}P = 4\pi\rho\omega^2 U_\infty a'(1-a)r^3\mathrm{d}r \tag{4.3}$$

From equation 4.3 it can inferred that at a given spanwise station, and for fixed rotational and inflow speeds, the power is maximized when the expression $f = a'(1-a)$ is maximum. Requiring that $\frac{\mathrm{d}f}{\mathrm{d}a} = 0$ yields the following equation:

$$\frac{\mathrm{d}a'}{\mathrm{d}a} = \frac{a'}{1-a} \tag{4.4}$$

Since the lift force is perpendicular to the relative inflow speed, and the induced speeds need to be parallel to the lift force (see figure 4.1), the following relation can be found:

$$x^2 a'(1+a') = a(1-a) \tag{4.5}$$

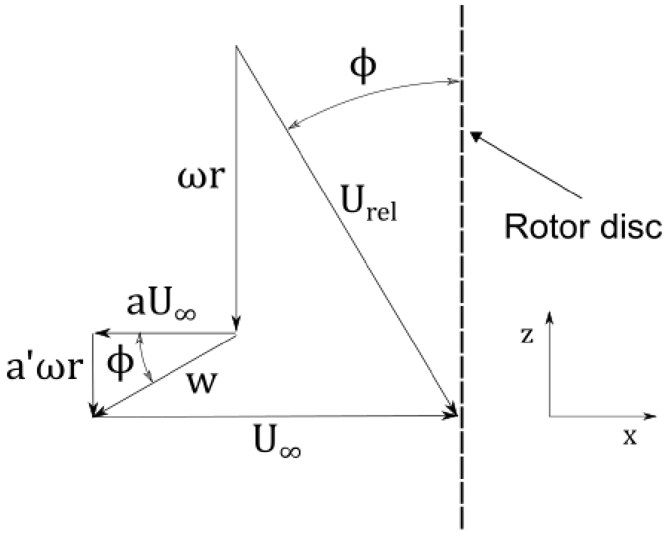

Figure 4.1: Decomposition of velocities at a spanwise section of the wing. [To be substituted by own figure, extracted from Hansen [2015]]

Where x is the equivalent of a local tip-speed ratio, defined as $x = \frac{\omega r}{u_\infty}$. The objective is to find the optimum value of a and a' for different spanwise positions of the blade. For this, equation 4.5 is differentiated with respect to a, yielding:

$$x^2(1+2a')\frac{\mathrm{d}a'}{\mathrm{d}a} = 1-2a \tag{4.6}$$

Now, equations 4.3, 4.5 and 4.6 can be combined to find the optimal values of induction for every value of x — therefore for every spanwise location. For an inflow of $u_\infty = 10m/s$, TSR = 6 and a maximum span of 1m, as will be used later in the optimization sections, the induction factors can be seen in figure 4.3

Knowing the ideal induction factors allows immediately to calculate what will be the ideal twist. Looking back at figure 4.1 the inflow angle can be computed as:

$$\phi = \arctan\left(\frac{1-a}{(1+a')x}\right) \tag{4.7}$$

Which are values now known. Then, the twist (in degrees) is computed as in equation 4.8. The relation between angles is as defined in figure 4.2.

$$\theta = \phi - \alpha_{opt} \tag{4.8}$$

Note that in (simple) BEM theory the airfoil sections are considered to retain their 2D lift and drag coefficients. Therefore, the optimal angle of attack α_{opt} will be the value that has a higher lift to drag ratio of the chosen 2D airfoil. This is an assumption not necessarily true in general; the three-dimensional effects will cause that the same airfoil presents different lift and drag coefficients along the span.

By equating the thrust (axial force) for momentum and blade element expressions the expression 4.9 can be obtained for the chord as a function of known values. The exact development requires the explanation of blade element theory and will not be presented here but can be consulted for example in Hansen [2015].

$$c = \frac{8\pi \mathrm{R}\cdot \mathrm{F}\cdot a\cdot x\cdot sin^2(\phi)}{(1-a)B\cdot \mathrm{TSR}\cdot C_n} \tag{4.9}$$

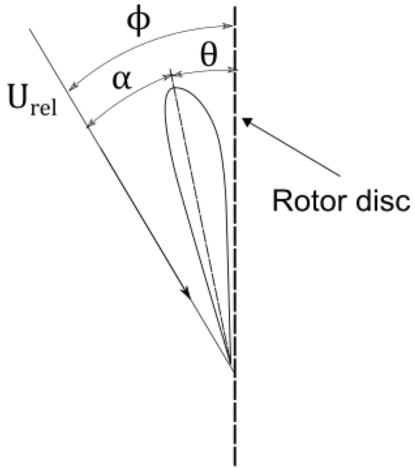

z

Figure 4.2: Relation between angle of attack, inflow angle and twist.

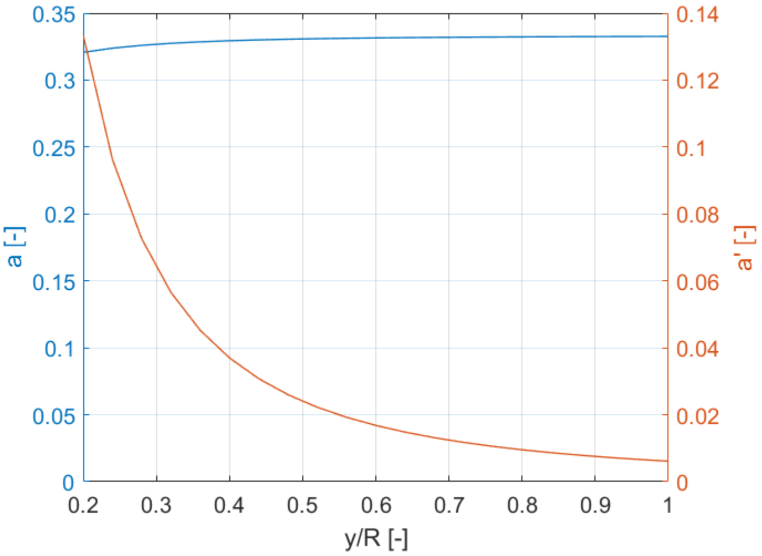

Figure 4.3: Optimal axial and tangential inductions as calculated with Glauert's theory.

In expression 4.9 B is the number of blades, in the example case 3. C_n is the normal coefficient of force obtained using the projections of $C_{l_{opt}}$ and $C_{d_{opt}}$. F is Prandtl's tip-loss factor. It accounts for the fact that the induction won't be homogeneous in the rotor, as would in a rotor with infinite blades, which has been considered until now. Prandtl's correction is, however, an approximation and it will be shown later on that the losses don't correspond exactly with what is predicted using panel methods (see section 4.2).

Figures 4.5 and 4.4 show the optimal chord and twist distributions. Prandtl's loss factor has been applied also at the root, as explained in Burton et al. [2011] to account for root losses as well as tip losses.

4.2. Analysis of Glauert's rotor using Panel Methods

In this subsection the Glauert rotor is analyzed using panel methods. The free wake and fixed wake models are compared against each other and against the BEM prediction. First,

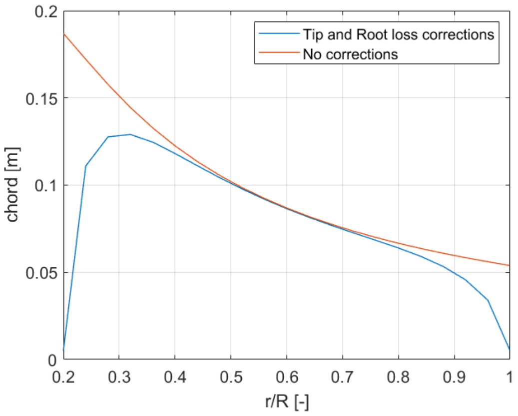

Figure 4.4: Ideal chord as calculated using Glauert's theory, with and without root and tip corrections applied.

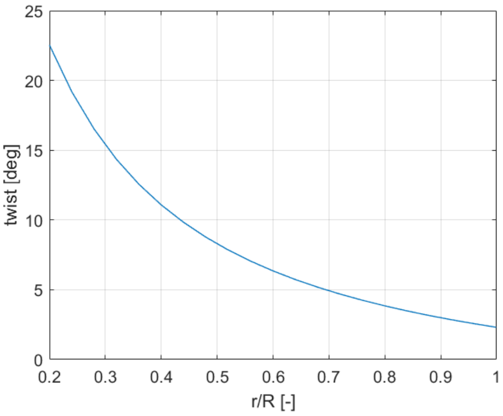

Figure 4.5: Ideal twist distribution as calculated using Glauert's theory.

look at figure 4.6: the prediction using BEM theory does not have the same magnitude as the prediction using the free wake model. The most noticeable differences are at the root, where the shape of the induction curve is significantly different for the analytical and computed results. This is due to the loss model of the BEM method: to correct for the assumption that the rotor has an infinite number of blades the Prandtl tipp loss correction factor has been applied; however, this model is not accurate enough (especially towards the root) to account for the losses originated because of the finite number of blades.

In the BEM model, as has been seen previously (see equation 4.3), the power is directly related to the induction. However, not necessarily so in for the panel method model, since the assumptions of the models are not the same. Remarkably, remember that BEM assumes that individual sections of the blade are independent from each other, which is not true in the panel method case and in general. This way, even though the induction is not the same for the two models, they present a remarkable similarity for the spanwise moments around the x axis, and therefore the power output (see figure 4.7). The tendency in this case is very similar for BEM and the free wake; however, close to the root and the tip the two models present some differences.

Lastly, it should be remarked that the fixed wake model is able to achieve similar results to the free wake model, provided that an appropriate value for sf is chosen. The difficulty resides in choosing the correct value for sf, which is not known in advance and can only be found by comparing the loads of a specific sf to the free wake loads.

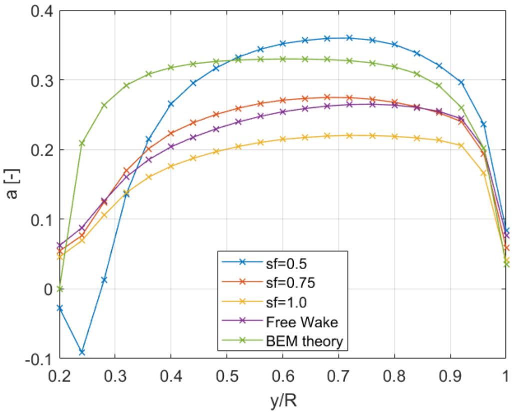

Figure 4.6: Axial induction in the glauert blade as computed with panel methods and BEM theory.

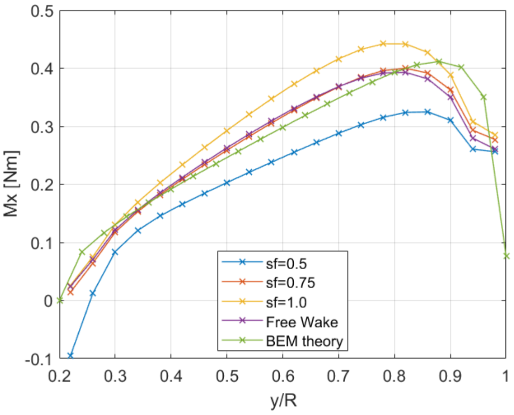

Figure 4.7: Moment around the x axis for the glauert blade as computed with panel methods and BEM theory.

5

Aerodynamic Optimization

In this chapter the aerodynamic optimization of a wind turbine blade is carried out using the modelling tools from chapter 3. The search strategy, regularization and parameterization are explained.Three optimization problems, with different constraints, are described. The optimizations are carried out using a fixed wake and the resulting geometries are analyzed using the free wake model.

5.1. Setup of the Optimization

5.1.1. Operating conditions

For the simulations that will be presented here below, the operating conditions of the wind turbine are set to be the same to facilitate comparison among them. These can be consulted in table 5.1

Table 5.1: Operating conditions of the wind turbines set for the optimization problems.

Air density	1.225kg/m^3
Inflow speed	10m/s
Yaw misalignment	0 deg
Tip Speed Ratio	6

Apart from the aforementioned conditions, the inflow is considered to be uniform and perpendicular to the rotor disc.

5.1.2. Discretization of the blade

The discretization of the blade is also kept constant for the different optimization runs to be able to compare among them. Prior to conducting the optimization of the blades, a convergence study was conducted on the spanwise loads to determine the mesh size required for the runs. This small study is presented in appendix A. The mesh parameters used in this optimization chapter are presented in table 5.2.

5.2. Parameterization

The blade is parameterized using NACA profiles. As such, it is possible to use as variables the maximum camber, position of maximum camber, thickness, twist and chord of the air-

Table 5.2: Mesh discretization parameters employed for optimization.

chord panels	80
span panels	20
wake revolutions	6
panels per revolution	18

foil. The variables are represented respectively as $[\boldsymbol{m}, \boldsymbol{p}, \boldsymbol{t}, \boldsymbol{c}]$ in figure 5.1, while the twist was defined previously in figure 4.2. The three first variables define the shape of the airfoil and have been predefined for the analysis. The chosen airfoil is the NACA 4412, which corresponds to a 4% maximum camber, located at 40% of the chord, and 12% of maximum thickness (percentages defined with respect to the chord). In order to keep the design comprehensible and easy to interpret, the choice of active variables has been restricted to the chord and the twist. The simulations done in this work will have as a purpose understand the role of these two variables in the design of a wind turbine blade. The other variables could be included at a later stage of the research, but it is first important to comprehend how the model behaves and if the optimizer takes advantage of any features of the model.

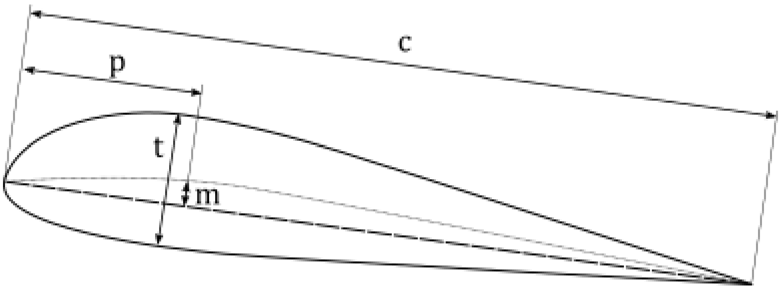

Figure 5.1: Representation of the parameterization of an airfoil using the NACA 4 digit series.

5.3. Filtering

The variables used in this work, as defined in the previous section 5.2, are independent from each other in each section. To prevent the appearance of non-physical solutions, or drastic changes in the design variables from one spanwise section to another, it is important to regularize the variables. Different kinds of filtering techniques exist for gradient based optimization. Sigmund [2007] presents several of those techniques for topology optimization, including the density filter used in this work, which was previously implemented in the work by Conlan-Smith et al. [2020] and is reproduced below for clarity:

In the density filter, the filtered design variables ($\tilde{\rho}$) are given by :

$$\tilde{\rho} = \boldsymbol{W}\rho \tag{5.1}$$

Where $\boldsymbol{W}$ is the density filter and can be computed as follows:

$$\boldsymbol{W}_{ij} = \frac{1}{\sum_{k=1}^{N_s} w_{ik}} w_{ij} \text{ where } w_{ij} = \max\left[0, R - d_{ij}\right] \tag{5.2}$$

The density filter is defined by a characteristic distance R. The value of a variable will be influenced by its neighbours proportionally as long as they are within that distance R.

The filtered vector of variables $\tilde{\rho}$ becomes an averaged version of the vector ρ. The effect of applying a filter is that there are no drastic changes in the design variables in the spanwise direction.

5.4. Search strategy and sensitivities

In the literature study of chapter 2 different search strategies have been described. Among those, in this work a gradient based search is used, specifically the algorithm used in this work is the Method of Moving Asymptotes (MMA) developed by Svanberg [1987]. MMA uses the variable values of the last two iterations as well as gradient information at the current step to update the variables. This section describes how these gradients are obtained to be able to feed them to MMA. It is necessary to compute the total derivative of the objective function f described in section 5.6:

$$\frac{\mathrm{d}f}{\mathrm{d}\boldsymbol{x}} = \frac{\partial f}{\partial \boldsymbol{x}} + \frac{\partial f}{\partial \boldsymbol{\mu}}\frac{\mathrm{d}\boldsymbol{\mu}}{\mathrm{d}\boldsymbol{x}} \tag{5.3}$$

Where μ here is a state variable (the doublet strength) and x to the design variables. The partial derivatives can be computed analytically with relative ease; however, not so the total derivatives. Enforcing that the residuals of the state equations must be equal to zero will allow to write $\frac{\mathrm{d}\mu}{\mathrm{d}x}$ only as a function of the partial derivatives of the resiual:

$$\frac{\mathrm{d}\boldsymbol{R}}{\mathrm{d}\boldsymbol{x}} = \frac{\partial \boldsymbol{R}}{\partial \boldsymbol{x}} + \frac{\partial \boldsymbol{R}}{\partial \boldsymbol{\mu}}\frac{\mathrm{d}\boldsymbol{\mu}}{\mathrm{d}\boldsymbol{x}} = 0 \tag{5.4}$$

$$\frac{\mathrm{d}\boldsymbol{\mu}}{\mathrm{d}\boldsymbol{x}} = -\left[\frac{\partial \boldsymbol{R}}{\partial \boldsymbol{\mu}}\right]^{-1}\frac{\partial \boldsymbol{R}}{\partial \boldsymbol{x}} \tag{5.5}$$

Hence, the derivative of the objective function can be computed also using only partial derivatives.

$$\frac{\mathrm{d}f}{\mathrm{d}\boldsymbol{x}} = \frac{\partial f}{\partial \boldsymbol{x}} - \frac{\partial f}{\partial \boldsymbol{\mu}}\left[\frac{\partial \boldsymbol{R}}{\partial \boldsymbol{\mu}}\right]^{-1}\frac{\partial \boldsymbol{R}}{\partial \boldsymbol{x}} \tag{5.6}$$

Note that the inverse of the matrix term $\left[\frac{\partial \boldsymbol{R}}{\partial \boldsymbol{\mu}}\right]$ is not actually computed. Instead, the following system of linear equations is solved for λ:

$$\left[\frac{\partial \boldsymbol{R}}{\partial \boldsymbol{\mu}}\right]^{\mathrm{T}}\boldsymbol{\lambda} = \left[\frac{\partial \boldsymbol{R}}{\partial \boldsymbol{x}}\right]^{\mathrm{T}} \tag{5.7}$$

And then the vector $\boldsymbol{\lambda}$ is substituted into equation 5.6, which can be rewritten:

$$\frac{\mathrm{d}f}{\mathrm{d}\boldsymbol{x}} = \frac{\partial f}{\partial \boldsymbol{x}} - \boldsymbol{\lambda}^{\mathrm{T}}\frac{\partial \boldsymbol{R}}{\partial \boldsymbol{x}} \tag{5.8}$$

Now that $\frac{\mathrm{d}f}{\mathrm{d}\boldsymbol{x}}$ is known, the derivative of the objective function with respect to the design variables $\boldsymbol{\rho}$ can be computed using the chain rule:

$$\frac{\mathrm{d}f}{\mathrm{d}\boldsymbol{\rho}} = \frac{\mathrm{d}f}{\mathrm{d}\boldsymbol{x}}\frac{\mathrm{d}\boldsymbol{x}}{d\tilde{\boldsymbol{\rho}}}\frac{d\tilde{\boldsymbol{\rho}}}{d\boldsymbol{\rho}} = \frac{\mathrm{d}f}{d\boldsymbol{x}}\frac{\mathrm{d}\boldsymbol{x}}{\mathrm{d}\tilde{\boldsymbol{\rho}}}\boldsymbol{W} \tag{5.9}$$

Where $\boldsymbol{\rho}$ is the vector of design variables, $\tilde{\boldsymbol{\rho}}$ are the filtered variables.

5.5. Validation of the Optimization

When using the fixed wake model to optimize the blade shape, the main assumption made is that the wake shape does not change between iterations. In this subsection an effort is made to proof or disproof this assumption by comparing the analytical fixed wake sensitivities to finite difference sensitivities from the free wake model.

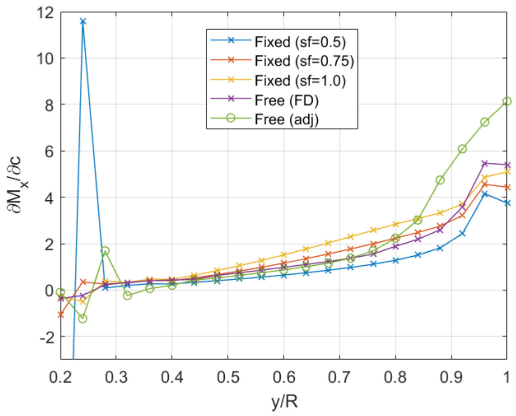

Figure 5.2: Sensitivities of M_x with respect to the chord for different fixed wake models and the free wake model computed for the Glauert optimal blade.

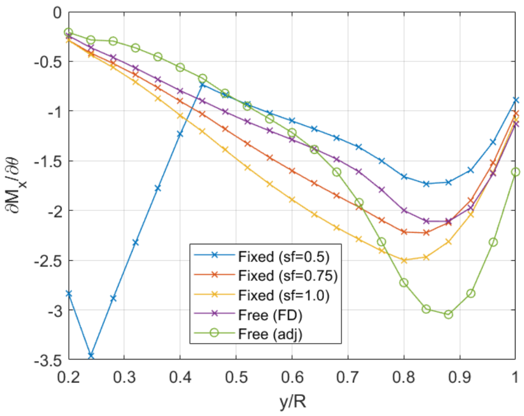

Figure 5.3: Sensitivities of M_x with respect to the twist for different fixed wake models and the free wake model computed for the Glauert optimal blade.

Figures 5.2 and 5.3 show the sensitivities of M_x (the objective function) with respect to the design variables, the chord and twist respectively. The sensitivities of the free wake model computed with the Finite Difference (FD) method are known to be correct and will be used as a reference, so they can be used for comparison and validation of the other sensitivities. For the FD approach the variables (normalized from 0 to 1) have been varied with a step of $1 \cdot 10^{-5}$, in the range for which the FD method typically presents less error (see the book by [Martins and Ning, 2021] for insight on the typical error related to FD approaches).

First of all, notice that the sensitivities computed using the analytical adjoint method (denoted as 'adj' in the figures) are very different from the FD values for the free wake model. The adjoint sensitivities of the free wake model are computed disregarding the change in wake shape between iterations completely; judging from the results in the figures this approach is not recommended since the differences are notable, especially towards the tip of the blade. It is concluded here that in order to use the free wake model to optimize wind turbine blades the changes of shape of the wake must be accounted for in the sensitivity calculation.

Regarding the fixed wake method, similarly to what was seen in section 4.2, how similar the fixed wake sensitivities are to the reference ones will depend on the value of sf. Also in section 4.2 it was shown that specifically for the Glauert blade $sf = 0.75$ yielded loads very similar to the free wake ones. Similarly here, different values of sf will give sensitivities that are in magnitude more or less close to the reference ones; nonetheless, none of them will mimic precisely the shape of the reference sensitivity curves. This indicates that the results of an optimization run obtained using a fixed wake will be different than those obtained using a free wake model.

Note that the sensitivities have been computed for a specific blade shape, namely the

Glauert blade. This exemplifies that choosing the appropriate value of sf allows to have sensitivities that are similar in magnitude to those of the free wake model. However, this approach cannot be used as a general proof that the fixed wake sensitivities are equivalent to the free wake ones, and also it has been seen in this example that the *shape* of the spanwise sensitivities is different for the fixed wake than it is for the free wake.

5.6. Definition and results of the optimization problems

The optimization is performed for a specific inflow speed and TSR. This means that the rotational speed is fixed and hence, using the moment around the axis of rotation (M_x) as an objective function is equivalent to using the power produced (eq. 5.10). Similarly, a CoP optimization would be also equivalent since the rotor area is also kept constant.

$$CoP = \frac{P}{\frac{1}{2}\rho u_\infty^3 S_{rot}} = \frac{M_x \Omega}{\frac{1}{2}\rho u_\infty^3 S_{rot}} \tag{5.10}$$

Next two optimization problems are presented with different constraints and active variables:

Problem 1:

$$\begin{aligned} \max_{\boldsymbol{c},\boldsymbol{\theta}} \quad & M_x(\boldsymbol{c},\boldsymbol{\theta}) \\ \text{s.t.} \quad & c_{min} \leq \boldsymbol{c} \leq c_{max}, \\ & \theta_{min} \leq \boldsymbol{\theta} \leq \theta_{max} \end{aligned} \tag{5.11}$$

This problem is unconstrained to mimic how the Glauert optimal rotor is obtained in the first place, without contstraints of any kind. Wide limits are allowed on the design variables. This will allow to notice what are the weaknesses of the model and which constraints need to be introduced to be able to obtain a geometry that is realistic.

As will be seen later in the results, there is an inherent problem with allowing the chord or twist to vary unconstrained. Since stall is not modelled in a panel method model, the performance at high angles of attack is overpredicted. Similarly, if no constraints are imposed, the chord values tend to become very big. Therefore, a strategy needs to be implemented in order to keep a realistic design, in form of bounds on the variables or constraints. Problem 2 will intend to tackle these issues later on.

Figures 5.4 and 5.5 show the resulting geometry of the optimization problem 1 performed with a fixed wake model for different values of sf. Recall that sf defines the length of the wake. As was exemplified in section 4.2, with a fixed wake an equivalent loading of the blade can be obtained to that of a free wake model, but only if an appropriate sf is chosen. Here sf is chosen beforehand, so there is no guarantee that the value chosen will correspond to the obtained design at the end of the optimization. To solve this problem, the optimization should be run for a range of sf values, and the performance of the blade (in terms of spanwise loads) should be assessed only with a free wake model.

In this case the chord was allowed to vary between $c_{min} = 0.05$ and $c_{max} = 0.5$. Note that the chord reaches the maximum allowed value near the root of the blade for all values of sf (see figure 5.4). The twist is allowed to vary between $\theta_{min} = 0 deg$ and $\theta_{max} = 60 deg$, and it is observed that the optimizer tends to reach the minimum twist possible (see figure 5.5), which maximizes the local angle of attack of each section.

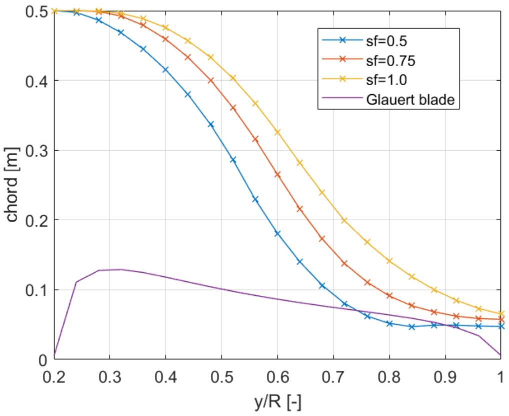

Figure 5.4: Problem 1: Spanwise chord distribution for different sf values.

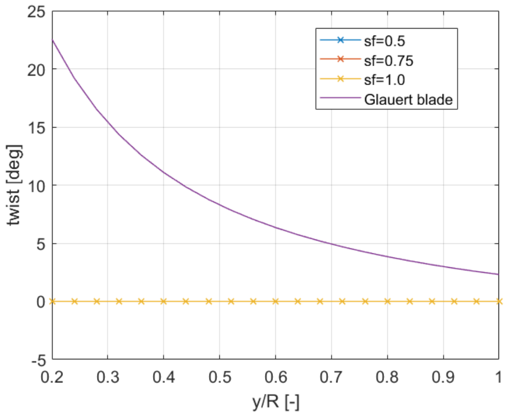

Figure 5.5: Problem 1: Spanwise twist distribution for different sf values.

It is apparent that the optimizer reaches unrealistic geometries when unconstrained and when the variables have wide bounds. One assumption made inherently here is that the change in shape of the blade will not affect the shape of the wake. This is erroneous, and it is difficult to determine how much this affects the outputs of the simulations. An attempt to assess this effect was done in section 5.5. An small value of sf is related to a wake which is closer to the blade and is also associated with higher axial induction values. Higher chord values are less desired in this case than it would be for a higher value of sf. Both the results from section 5.5 and from figure 5.4 agree on this.

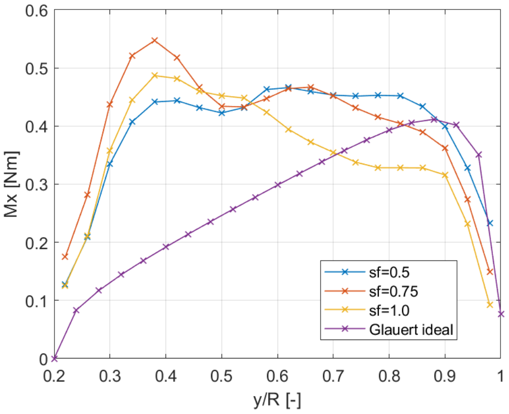

Figure 5.6: Problem 1: Spanwise moment distribution on the optimized blades. Loads computed using a free wake model.

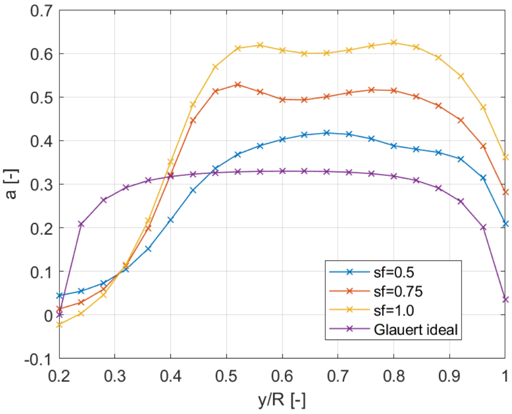

Figure 5.7: Problem 2: Spanwise axial induction on the optimized blades. Velocities computed using a free wake model.

The Betz limit states that the power of a wind turbine cannot go over $CoP = 16/27 \approx 0.59$. The performance of the three designed blades, when run on the free wake method, have performances that exceed this limit (see table 5.3). This can also be seen when comparing the spanwise moment generated by these blades as compared to the moment generated by the glauert blade (figure 5.6). Similarly, the axial induction (figure 5.7) of the designs is higher than the ideal induction calculated using momentum theory. All these results indicate that the panel method model is producing unrealistic results.

Table 5.3: Problem 1: performance of the three optimized blades in terms of power and coefficient of power.

Design	Power	CoP
sf = 0.5	1355.7	0.705
sf = 0.75	1392.5	0.724
sf = 1.0	1216.9	0.632

Problem 2:

$$\begin{aligned} \max_{\boldsymbol{c},\boldsymbol{\theta}} \quad & M_x(\boldsymbol{c},\boldsymbol{\theta}) \\ \text{s.t.} \quad & T \le T_{max}, \\ & c_{min} \le \boldsymbol{c} \le c_{max}, \\ & \theta_{min} \le \boldsymbol{c} \le \theta_{max} \end{aligned} \tag{5.12}$$

In this second problem the twist and chord are allowed to vary as well. However, to improve on the results from problem 1, the chord bounds have been limited to a smaller range ($c_{min} = 0.05$; $c_{max} = 0.15$). The thrust is now used as a constraint. This is appropriate because on one side, it is related to structural constraints on the tower —it is desirable to limit the thrust to have a reduced bending moment at the base of the tower, which in turn helps limit material usage on the tower—. On the other side, constraining the thrust will allow realistic twist curves to appear on the final designs.

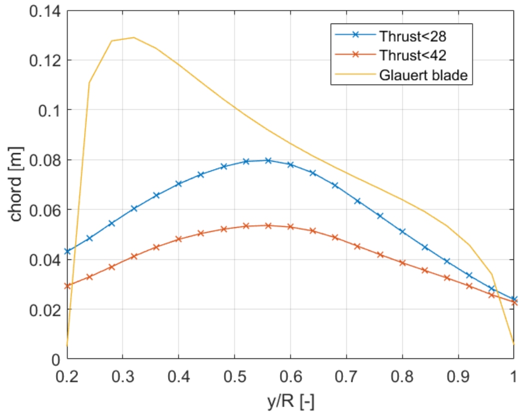

Figure 5.8: Problem 2: spanwise chord distribution for different thrust constraints; $sf = 0.5$.

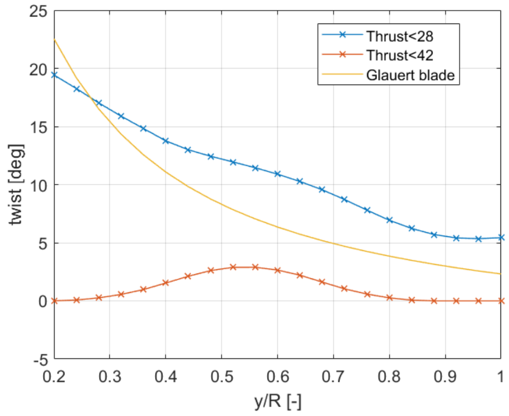

Figure 5.9: Problem 2: spanwise twist distribution for different thrust constraints; $sf = 0.5$.

Figures 5.8 to 5.13 show the geometries obtained for different sf values and thrust constraints for problem 2. The most important thing to note is that the thrust constraint is able to limit the twist values and produce realistic results in most cases. The spanwise chord distribution now resembles more that of a typical wind turbine blade as well.

In the theoretical case obtained using momentum theory the chord at the tip and the root of the blade tends to 0; however, the designs from panel method optimization consistently show chords of finite length towards the extremes of the blade.

The performance of the optimized designs is shown in table 5.4. The loads on the blades have been analyzed with a free wake model to compare their performance in terms of Coefficient of Power. The highest performing blade, according to the results, is the one produced using $sf = 0.5$ and T<42. Even though its power output seems realistic, this blade

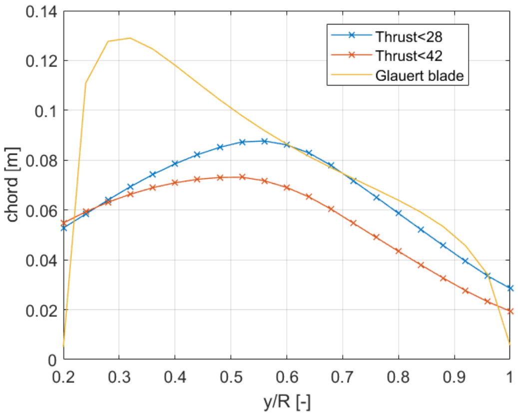

Figure 5.10: Problem 2: spanwise chord distribution for different thrust constraints; $sf = 0.75$.

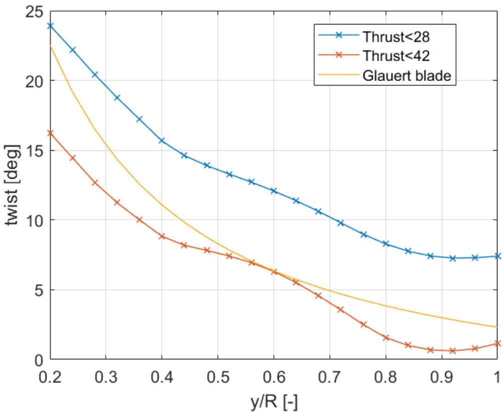

Figure 5.11: Problem 2: spanwise twist distribution for different thrust constraints; $sf = 0.75$.

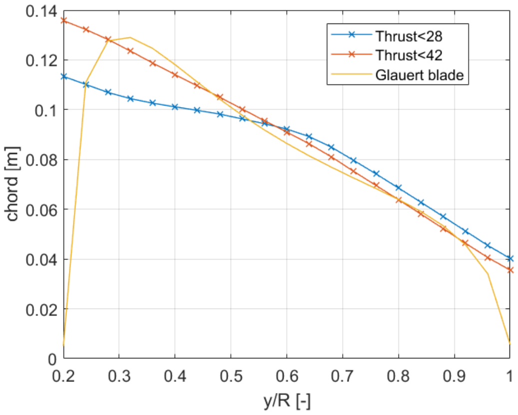

Figure 5.12: Problem 2: spanwise chord distribution for different thrust constraints; $sf = 1.0$.

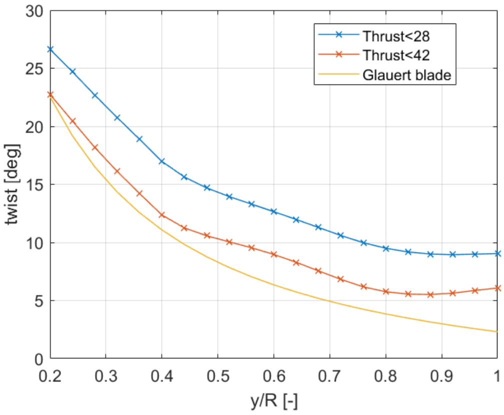

Figure 5.13: Problem 2: spanwise twist distribution for different thrust constraints; $sf = 1.0$.

performs better than the rest because the twist has become very low with the combination of parameters and constraints imposed. This means that the local angle of attack of the blade will very high towards the root of the blade, which as discussed previously is not punished in a panel method model. The local angle of attack of this particular blade is depicted in figure 5.14 to exemplify this effect. For angles of attack $\approx$ 15deg a 2D NACA 4412 airfoil would begin to stall. For similar reasons, it is difficult to assess whether the designs represent an improvement in performance to, for example, the Glauert blade. A higher order model that would take into account all physical phenomena, for example a CFD model, should ultimately be used to assess the performance of the obtained designs.

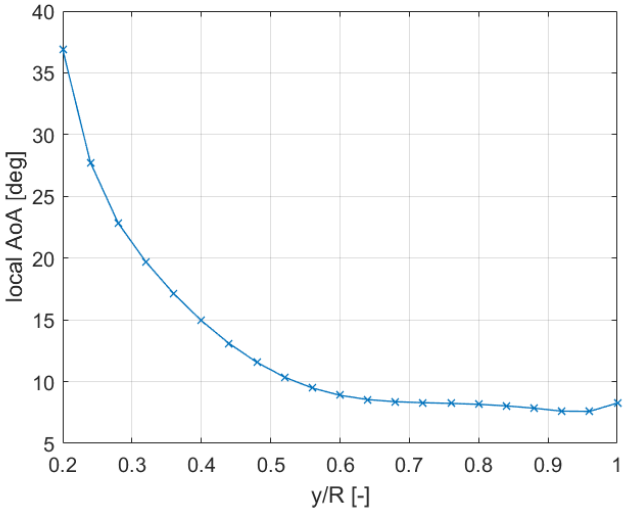

Figure 5.14: Problem 2: Local angle of attack of the blade obtained with T<42 and $sf = 0.5$.

Table 5.4: Problem 2: performance of the optimized blades in terms of power and coefficient of power.

Design	Constraint	Power	CoP
sf = 0.5	T<28	754.3	0.392
	T<42	945.8	0.492
sf = 0.75	T<28	702.8	0.365
	T<42	934.8	0.486
sf = 1.0	T<28	673	0.35
	T<42	899.2	0.467

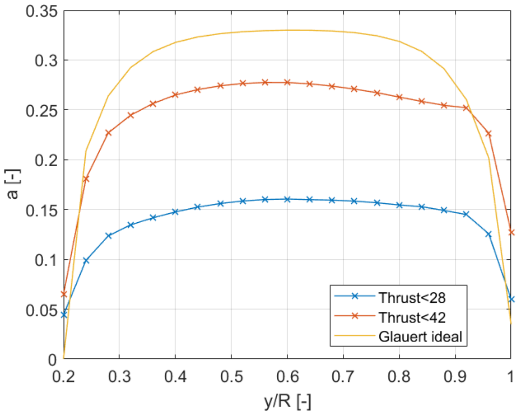

Figure 5.15: Problem 2: spanwise axial induction distribution for different thrust constraints; $sf = 0.5$.

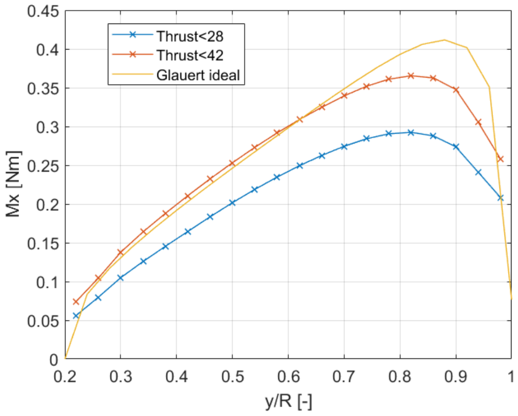

Figure 5.16: Problem 2: spanwise M_x distribution for different thrust constraints; $sf = 0.5$.

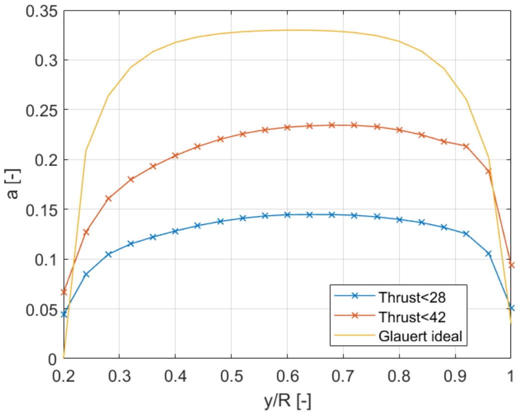

Figure 5.17: Problem 2: spanwise axial inductiond distribution for different thrust constraints; $sf = 0.75$.

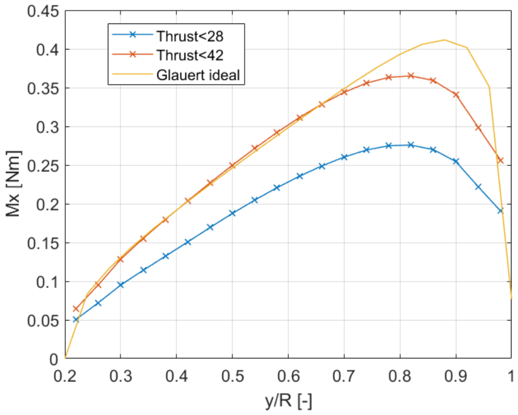

Figure 5.18: Problem 2: spanwise M_x distribution for different thrust constraints; $sf = 0.75$.

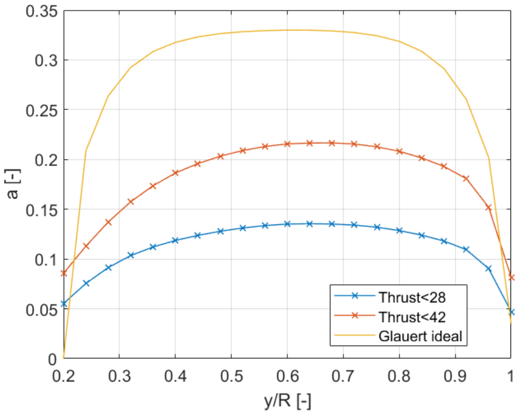

Figure 5.19: Problem 2: spanwise axial induction distribution for different thrust constraints; $sf = 1.0$.

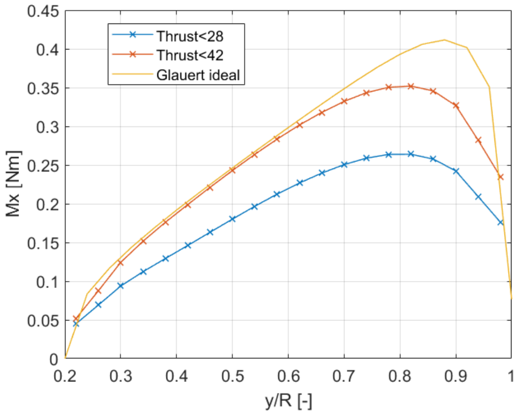

Figure 5.20: Problem 2: spanwise M_x distribution for different thrust constraints; $sf = 1.0$.

6

Conclusions and recommendations

This chapter reviews the most relevant results found throughout this thesis work and makes recommendations on improvements of the model and the analysis for future work to be done in the topic.

6.1. Conclusions

The aim of this thesis has been to assess the viability of panel methods to be used for gradient based optimization of wind turbine blades.

A panel method has been developed to calculate the spanwise loads —and therefore power— of horizontal axis wind turbines using a Dirichlet boundary condition. Both a fixed wake and free wake models have been developed for the wake and their validity has been assessed. The free wake model presents good agreement with previous panel method models, while the fixed wake only does so when the parameters of the model are chosen appropriately. However, the tangential loading is substantially different when compared to CFD computations; therefore, all designs should ultimately be assessed using a higher order model that accounts for viscosity and stall phenomena.

The optimum blade obtained using the Glauert model was chosen as a baseline and analyzed to be compared with the blades resulting from the optimization runs. This provided insights into the differences between momentum theory and panel methods; namely, the Prandtl tip loss correction, which is widely used in the literature, shows some differences compared to the losses computed with the panel model.

For the optimization, a simple model was chosen to evaluate the viability of the optimization using panel methods. Optimization runs for the fixed model were performed, using only the chord and twist as optimization variables to keep the model understandable. Unconstrained optimization shows to take advantage of the flaws of panel methods, namely the lack of stall modelling means that the model overpredicts the perfomance of high angles of attack and tends towards them. Applying appropriate bounds on the chord and twist variables, more realistic designs can be obtained, where the chord and twist lie within realistic bounds. However, a difficulty to assess the performance of the designs has been found. Because the performance is been assessed with a panel method itself any flaws in a panel method, therefore, are obviated when evaluating the performance, for example high angles of attack are viewed as very good.

To conclude, the obtained results show that viable designs are possible using panel methods for gradient based optimization, but only if appropriate bounds and constraints are applied to keep the model within the range of its applicability. Ultimately, the performance of the obtained designs should be assessed using higher order aerodynamic models.

6.2. Recommendations for future work

The optimization runs have been performed using the fixed wake model, which does not take into account the changes of shape in the wake when the geometry changes. To improve the optimization, the sensitivities of the wake geometry with respect to the changes in the design and state variables should be computed. While this would eliminate the variable of the wake shape, which has been present in this work, it still is not enough to deal with the limitations of panel methods. As has been mentioned throughout the work, panel methods are incapable of assessing properly the loads for high angles of attack. The solution applied in this work was a thrust constraint; however, it would be an improvement to apply a constraint on the local angle of attack of every section. Since the axial induction and the undisturbed inflow are known, it is possible to evaluate the angle of attack at every iteration and calculate the sensitivities.

Related to the applicability panel methods, it should be mentioned that the performance of the designs obtained has been assessed using a panel method again. Therefore, any flaws of the model exploited during the design will also be present during the posterior analysis. To properly assess how good the performance of these designs is, it should be done using a higher order model, e.g. CFD.

It is well known that C_P integration is not accurate enough for drag calculations [Katz and Plotkin, 2004], which might be critical when computing the tangential loads at the rotor — and therefore the power. While it is not completely clear exactly what effect this might have on the designed geometries, it is clear that the results will be affected if errors in the drag computation are present in the current designs. Using Trefftz Plane (TP) integration to compute the loads showed to yield better results for wing optimization in previous work Conlan-Smith et al. [2020] and seems to be the way to go for optimization of wings. However, to the knowledge of the author Trefftz plane (also called Far-field) integration has not been used plenty for wind turbines in panel methods. Unlike its use for wings, where the expressions to calculate lift and induced drag are well known [Drela, 2014], using Trefftz plane integration in this case would therefore require to develop the analytical expressions for force integration, followed by a validation analysis, prior to implementing TP integration for optimization purposes. This analysis had to be excluded of this thesis work for time reasons only, but it is strongly encouraged for future investigations to inquire further into far-field integration. Something to note with regards to TP integration is that it employs the velocity field on the wake of a wind turbine. This calculations have shown to be imprecise for the explicit free wake model, which might be an issue for this kind of implementation.

The choice of objectives in this work has been based on simplicity. For an early stage of development of a model it is better to chose simple models that can be understood, and hence the choice of M_x as an objective function made sense this way. However, this does not reflect completely on what makes a turbine optimal when it comes to a real life business case. For that purpose, it would be more appropriate to use Cost of Energy as an objective function [Bottasso et al., 2016]. Deep knowledge of the cost of materials, manufacturing, transporting, maintenance costs, etc. is required to calculate COE as a function of the design variables, and so this task also came to be out of the scope of this work. Similarly, for the choice of constraints it would be better to use Design load cases as required when a real wind turbine is designed.

The studies conducted here have used only the twist and chord as variables to optimize. The reason is that it becomes easier to interpret the results obtained this way, but it would be possible to use the other NACA parameters as variables with no further implementations with the current code. This would allow the optimizer to effectively be able to choose freely between different NACA profiles at every section.

Finally, with the developed aerodynamic model and following the steps of the work by Conlan-Smith [2020], it would be possible to couple the aerodynamic optimizer to a structural model to perform aerostructural optimization.

A

Effect of Discretization on the loads

This section presents a simple study of the effect of the discretization on the spanwise loads of a wind turbine. Figures A.1 to A.8 present the tangential and normal forces on a sample wind turbine rotor employing a fixed wake for the discretization, using the parameters of table as a baseline A.1 and changing the relevant parameter for every plot. From the figures it is apparent that the discretization does not have a great effect on the tangential forces for the tested meshes. Furthermore, it is considered that the normal spanwise loadings converge at the following discretization: 80 chordwise panels, 20 spanwise panels, 10 wake revolutions and 36 wake panels per revolution (10 deg. of spacing between wake panels).

Table A.1: Baseline discretization used for comparison with other coarser and finer meshes.

chord panels	80
span panels	20
wake revolutions	10
panels per revolution	18

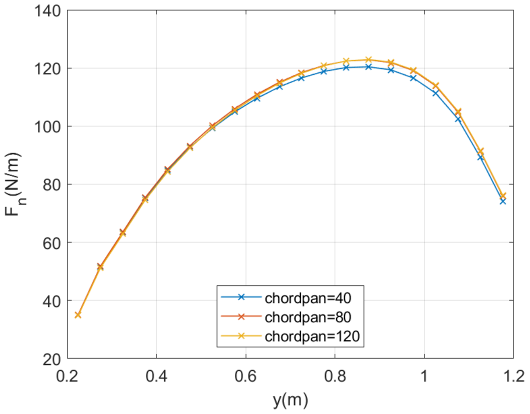

Figure A.1: Normal force to the rotor along the span for different chord discretizations.

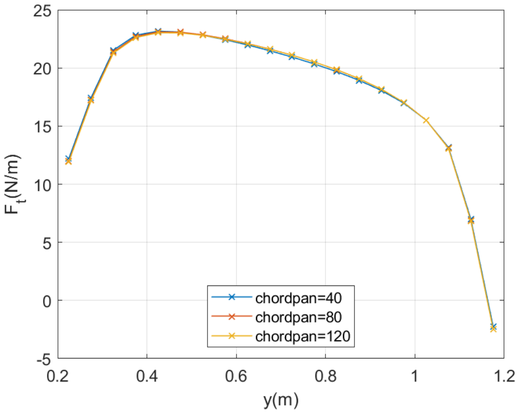

Figure A.2: Tangential force to the rotor along the span for different chord discretizations.

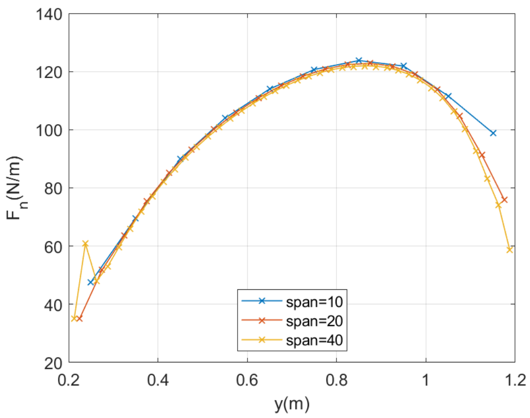

Figure A.3: Normal force to the rotor along the span for different spanwise discretizations.

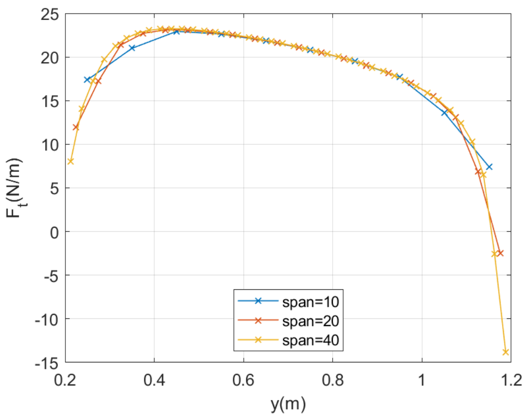

Figure A.4: Tangential force to the rotor along the span for different spanwise discretizations.

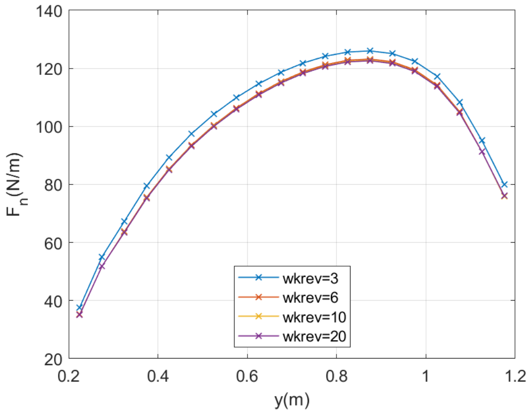

Figure A.5: Normal force to the rotor along the span for different number of wake revolutions.

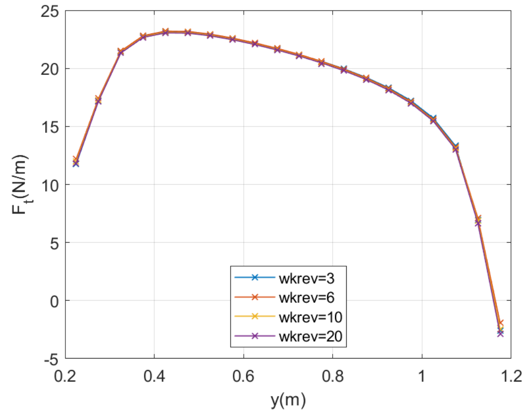

Figure A.6: Tangential force to the rotor along the span for different number of wake revolutions.

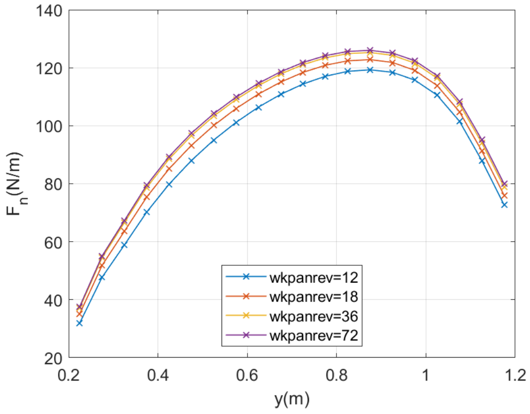

Figure A.7: Normal force to the rotor along the span for different number of wake panels per revolution.

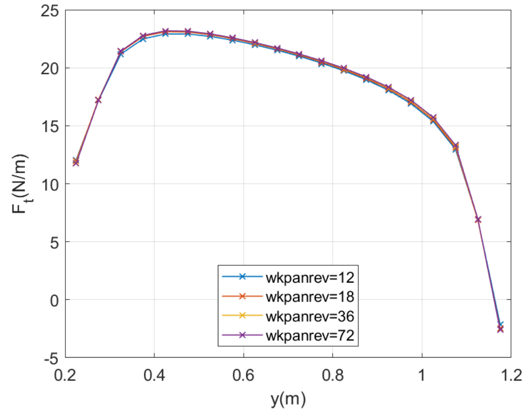

Figure A.8: Normal force to the rotor along the span for different number of wake panels per revolution.

B

Finite Difference checks

A finite difference check has been done to ensure that the analytical sensitivities are properly calculated. The way this check works is the following: the value of the objectives and constraints is calculated using the developed aerodynamic model (which has been previously validated) for a specific blade geometry; then the variables are perturbed by a given increment $\Delta\rho$ such that the derivative of the objective can be approximated using expression B.1 — similarly for the constraint function and its derivatives.

$$\frac{\mathrm{d}f}{\mathrm{d}\rho} \approx \frac{\Delta f}{\Delta\rho} \tag{B.1}$$

A finite difference scheme to calculate sensitivities is accurate for a specific step size, but becomes inaccurate when the step is too low (due to machine accuracy) and when the step is too high (because the approximation of equation B.1 does not hold). The error of a finite difference scheme plotted against the $\Delta\rho$ perturbation then follows a characteristic 'V' shape. More insights into finite difference calculation can be seeked in Martins and Ning [2021]. Then, assuming that the sensitivities calculated using the analytic adjoint method are correct, the difference between the adjoint sensitivities and the finite difference computations should resemble this 'V' shape as well. This is what can be seen in figures B.1 and B.2 for the objective and constraint sensitivities, respectively, of the fixed wake model. Every line corresponds to the mentioned relative error for a specific variable of the blade. In this case both the twist and the chord variables are shown for every section of the blade. The finite difference check ensures that the aerodynamic model and its derivatives coincide, but it is still necessary to ensure that the model itself is correct to be able to claim that the sensitivities point in the right direction.

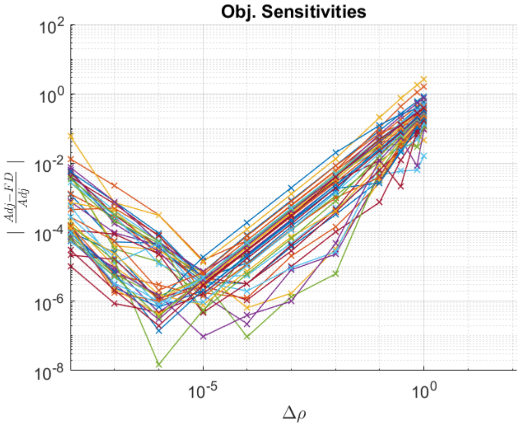

Figure B.1: Relative error between the finite difference sensitivities and the adjoint sensitivities for the objective function.

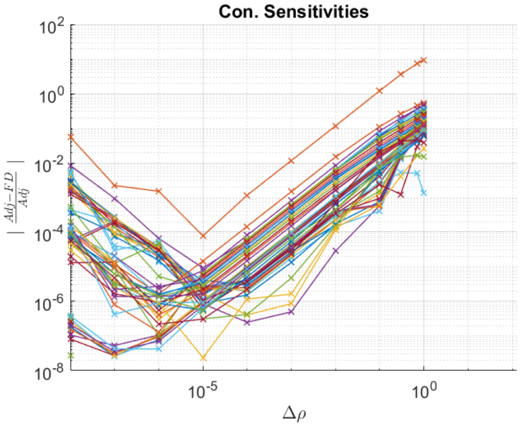

Figure B.2: Relative error between the finite difference sensitivities and the adjoint sensitivities for the constraint functions.

C

Code structure and contribution

This thesis departs from previous work done in the ambit of optimization of aircraft wings (see Conlan-Smith [2020]). Therefore, at the start of this thesis work a software already existed that could analyze the loads on a wing and perform aerodynamic and aerostructural optimization. The additions that have been made to the software during this work can be summarized in the next points:

1. Geometry input
2. Rotational symmetry
    - Influence coefficients and their derivatives
    - Computation of the velocity field at the wake
3. Velocity field
    - Source terms and their derivatives
    - Load calculations and their derivatives
4. Wake modeling
    - New wake geometry
    - New scheme implemented with the Free-wake model
5. New objectives and constraints

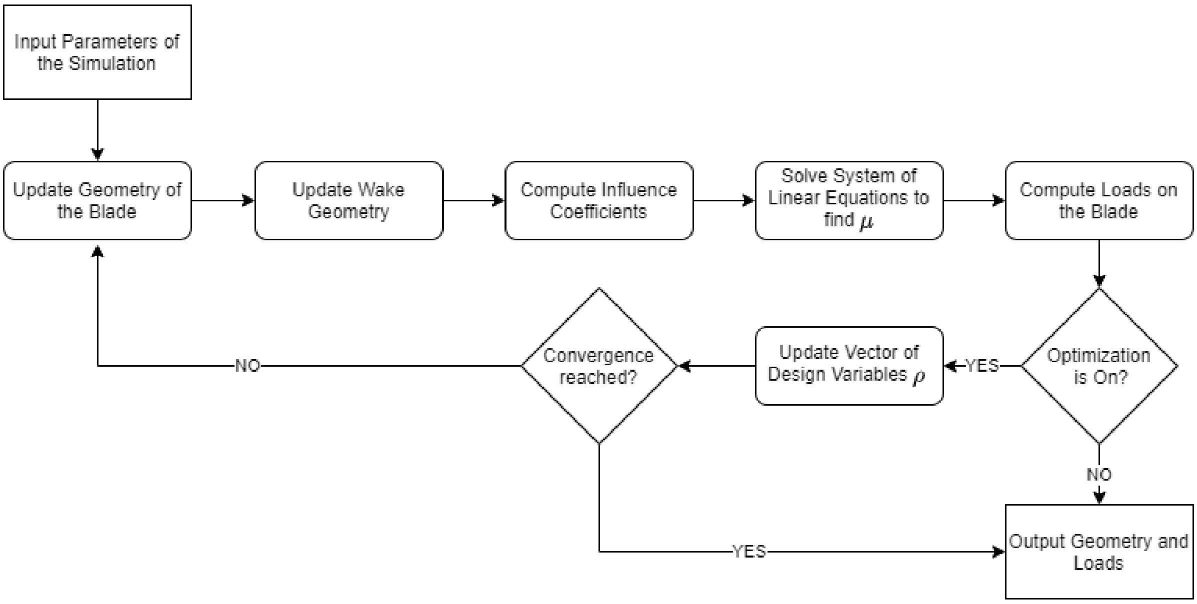

Figure C.1: Flowchart of the code.

Bibliography

J. Anderson. *Fundamentals of Aerodynamics, Sixth Edition.* 2017.

T. Ashuri, M. B. Zaaijer, J. R.R.A. Martins, G. J.W. van Bussel, and G. A.M. van Kuik. Multidisciplinary design optimization of offshore wind turbines for minimum levelized cost of energy. *Renewable Energy*, 68, 2014. ISSN 09601481. doi: 10.1016/j.renene.2014.02.045.

F. Blondel, R. Boisard, M. Milekovic, G. Ferrer, C. Lienard, and D. Teixeira. Validation and comparison of aerodynamic modelling approaches for wind turbines. In *Journal of Physics: Conference Series*, volume 753, 2016. doi: 10.1088/1742-6596/753/2/022029.

C. L. Bottasso, A. Croce, L. Sartori, and F. Grasso. Free-form design of rotor blades. In *Journal of Physics: Conference Series*, volume 524, 2014. doi: 10.1088/1742-6596/524/1/012041.

C. L. Bottasso, P. Bortolotti, A. Croce, and F. Gualdoni. Integrated aero-structural optimization of wind turbines. *Multibody System Dynamics*, 38(4), 2016. ISSN 1573272X. doi: 10.1007/s11044-015-9488-1.

Tony Burton, Nick Jenkins, David Sharpe, and Ervin Bossanyi. *Wind Energy Handbook, Second Edition.* 2011. doi: 10.1002/9781119992714.

C. Conlan-Smith, N. Ramos-García, O. Sigmund, and C. S. Andreasen. Aerodynamic Shape Optimization of Aircraft Wings Using Panel Methods. *AIAA Journal*, 58(9):3765–3776, 9 2020. ISSN 0001-1452. doi: 10.2514/1.J058979. URL `https://arc.aiaa.org/doi/10.2514/1.J058979`.

Cian Conlan-Smith. *Aerodynamic and Aeroelastic Shape Optimization of Aircraft Wings.* PhD thesis, Technical University of Denmark, 2020.

Cian Conlan-Smith and Casper Schousboe Andreasen. A coupled 3D panel-beam model for aeroelastic optimization of aircraft wings. *AIAA Journal*, Accepted/In Press, 2020.

Mark Drela. *Flight Vehicle Aerodynamics.* 2014.

Gunter Reinald Fischer, Timoleon Kipouros, and Anthony Mark Savill. Multi-objective optimisation of horizontal axis wind turbine structure and energy production using aerofoil and blade properties as design variables. *Renewable Energy*, 62:506–515, 2 2014. ISSN 09601481. doi: 10.1016/j.renene.2013.08.009.

H. Glauert. Airplane Propellers. In *Aerodynamic Theory.* 1935. doi: 10.1007/978-3-642-91487-4{_}3.

GWEC. Global Wind Report 2019. Technical report, 2020. URL `https://gwec.net/global-wind-report-2019/`.

M. O.L. Hansen, J. N. Sørensen, S. Voutsinas, N. Sørensen, and H. Aa Madsen. State of the art in wind turbine aerodynamics and aeroelasticity, 2006. ISSN 03760421.

Martin O.L. Hansen. *Aerodynamics of wind turbines: Third edition*. 2015. doi: 10.4324/9781315769981.

John L. Hess. Calculation of potential flow about arbitrary three dimensional lifting bodies. Technical report, McDonnell Douglas, 1973.

IEA. *World Energy Outlook 2020*. 2020. URL `https://www.iea.org/reports/world-energy-outlook-2020#`.

Kai A. James, Graeme J. Kennedy, and Joaquim R.R.A. Martins. Concurrent aerostructural topology optimization of a wing box. *Computers and Structures*, 134, 2014. ISSN 00457949. doi: 10.1016/j.compstruc.2013.12.007.

J. Jonkman, S. Butterfield, W. Musial, and G. Scott. Definition of a 5-MW reference wind turbine for offshore system development. *Contract*, (February), 2009. ISSN 01487299.

J. Katz and A. Plotkin. Low-Speed Aerodynamics, Second Edition. *Journal of Fluids Engineering*, 126(2), 2004. ISSN 0098-2202. doi: 10.1115/1.1669432.

Gaetan K.W. Kenway, Graeme J. Kennedy, and Joaquim R.R.A. Martins. A CAD-free approach to high-fidelity aerostructural optimization. In *13th AIAA/ISSMO Multidisciplinary Analysis and Optimization Conference 2010*, 2010. doi: 10.2514/6.2010-9231.

Stephen Lawton and Curran Crawford. Investigation and optimization of blade tip winglets using an implicit free wake vortex method. In *Journal of Physics: Conference Series*, volume 524, 2014. doi: 10.1088/1742-6596/524/1/012033.

G. Leishman. *Principles of helicopter aerodynamics*. 2006.

R. M. Pinkerton. Calculated and measured pressure distributions over the midspan section of the NACA 4412 airfoil. Technical report, National Advisory Committee for Aeronautics, 1937.

Mads H.Aa Madsen, Frederik Zahle, Niels N. Sørensen, and Joaquim R.R.A. Martins. Multipoint high-fidelity CFD-based aerodynamic shape optimization of a 10 MW wind turbine. *Wind Energy Science*, 4(2), 2019. ISSN 23667451. doi: 10.5194/wes-4-163-2019.

Joaquim R.R.A Martins and Andrew Ning. *Engineering Design Optimization*. Working draft edition, 2021.

Bram Peerlings. A review of aerodynamic flow models, solution methods and solvers – and their applicability to aircraft conceptual design. Technical report, 2018.

N. Ramos-García, J. N. Sørensen, and W. Z. Shen. Validation of a three-dimensional viscous-inviscid interactive solver for wind turbine rotors. *Renewable Energy*, 70, 2014. ISSN 09601481. doi: 10.1016/j.renene.2014.04.001.

D. J. Robison, F. N. Coton, R. A.Mc D. Galbraith, and M. Vezza. Application of a prescribed wake aerodynamic prediction scheme to horizontal axis wind turbines in axial flow. *Wind Engineering*, 19(1), 1995. ISSN 0309524X.

Matias Sessarego and Wen Zhong Shen. Aero-structural optimization of wind turbine blades using a reduced set of design load cases including turbulence. In *Journal of Physics: Conference Series*, volume 1037, 2018. doi: 10.1088/1742-6596/1037/4/042018.

Matias Sessarego, Néstor Ramos-García, Hua Yang, and Wen Zhong Shen. Aerodynamic wind-turbine rotor design using surrogate modeling and three-dimensional viscous-inviscid interaction technique. *Renewable Energy*, 93, 2016. ISSN 18790682. doi: 10.1016/j.renene.2016.03.027.

Ole Sigmund. Morphology-based black and white filters for topology optimization. *Structural and Multidisciplinary Optimization*, 33(4-5), 2007. ISSN 1615147X. doi: 10.1007/s00158-006-0087-x.

K. Svanberg. The method of moving asymptotes - a new method for structural optimization. *International Journal for Numerical Methods in Engineering.*, 24(2), 1987.

Jesse Thé and Hesheng Yu. A critical review on the simulations of wind turbine aerodynamics focusing on hybrid RANS-LES methods, 2017. ISSN 03605442.

L.J. Vermeer, J.N. Sørensen, and A. Crespo. Wind turbine wake aerodynamics. *Progress in Aerospace Sciences*, 39(6-7), 8 2003. ISSN 03760421. doi: 10.1016/S0376-0421(03)00078-2.

Júlio Xavier Vianna Neto, Elci José Guerra Junior, Sinvaldo Rodrigues Moreno, Helon Vicente Hultmann Ayala, Viviana Cocco Mariani, and Leandro dos Santos Coelho. Wind turbine blade geometry design based on multi-objective optimization using metaheuristics. *Energy*, 162, 2018. ISSN 03605442. doi: 10.1016/j.energy.2018.07.186.

Tongguang Wang. A brief review on wind turbine aerodynamics. *Theoretical and Applied Mechanics Letters*, 2(6), 2012. ISSN 20950349. doi: 10.1063/2.1206201.

Zhijun Wang, Akke S.J. Suiker, Hèrm Hofmeyer, Twan van Hooff, and Bert Blocken. Coupled aerostructural shape and topology optimization of horizontal-axis wind turbine rotor blades. *Energy Conversion and Management*, 212, 2020. ISSN 01968904. doi: 10.1016/j.enconman.2020.112621.

Wind Europe. Wind energy in Europe in 2019. Technical report, 2020. URL `https://windeurope.org/data-and-analysis/product/wind-energy-in-europe-in-2019-trends-and-statistics/`.